

---

# SEQUENTIAL PHYSICS-CONSTRAINED NEURAL OPERATOR FORWARD MODELING FOR THE *Norne* RESERVOIR SYSTEM

---

Clement Etienam<sup>\*,\*</sup>

Juntao Yang<sup>1</sup>

Oleg Ovcharenko<sup>1</sup>

Nick Luiken<sup>1</sup>

Tsubasa Onishi<sup>1</sup>

Nefeli Moridis<sup>1</sup>

Issam Said<sup>1</sup>

## ABSTRACT

We develop a comprehensive mathematical and computational framework for sequential surrogate modeling of three-phase black-oil reservoir dynamics using neural operators, with particular emphasis on Fourier Neural Operators (FNO) and their physics-informed variant (PINO). The application focus is the Norne benchmark reservoir, defined on a heterogeneous  $46 \times 112 \times 22$  grid ( $N = 113,344$  cells), with a production history spanning  $T = 30$  timesteps covering 3298 days.

Our theoretical contributions are organized around four interlocking problems.

**(1) Functional-analytic formulation.** We embed the discrete-time black-oil system in a rigorous product-Sobolev-space setting. The finite-volume implicit residual operator  $R : \mathbb{R}^{4N} \times \mathbb{R}^{4N} \rightarrow \mathbb{R}^{4N}$  is the canonical mathematical object bridging simulator physics to neural-operator training; its zero set  $\mathcal{M}$  defines the *physics-consistent manifold* on which PINO training concentrates predictions. We prove well-posedness of the implicit timestep map  $\mathcal{F}$  under a discrete coercivity condition (Theorem 2.6), provide sharp local Lipschitz estimates (Lemma 2.7), and characterize the elliptic-hyperbolic structural dichotomy that governs differential stability across state variables.

**(2) Covariate shift and distributional divergence.** We prove that the Wasserstein-2 distance between the true-state distribution  $\mu_n$  and the predicted-state distribution  $\hat{\mu}_n^\theta$  grows as  $W_2(\hat{\mu}_n^\theta, \mu_n) \leq \varepsilon(L^n - 1)/(L - 1)$ , where  $L$  is the operator Lipschitz constant and  $\varepsilon$  the one-step error (Theorem 4.1). We further bound the resulting population-risk discrepancy between one-step and autoregressive training paradigms (Corollary 4.2) and show this gap drives exponential  $R^2$  degradation for  $L > 1$  hyperbolic variables.

**(3) Physics-constrained spectral stability.** We prove that PINO training with physics weight  $\lambda_R \geq \lambda_R^*$  reduces the spectral radius of the learned operator’s Jacobian to  $\varrho(D_x \mathcal{G}_\theta) \leq \rho_{\mathcal{F}} + C\lambda_R^{-1/2}$ , where  $\rho_{\mathcal{F}} < 1$  is the dissipativity rate of the true dynamics (Theorem 6.5). A companion result (Theorem 6.6) establishes that the PINO residual penalty acts as a spectral Jacobian regularizer: it penalizes deviations of  $D_x \mathcal{G}_\theta$  from the true dynamics Jacobian  $D_x \mathcal{F}$  in a weighted operator norm, with error  $\mathcal{O}(\lambda_R^{-1/2})$ . Combining these, we prove a uniform-in-time rollout error bound  $\|\delta_n\|_\phi \leq \varepsilon/(1 - \rho)$  for PINO-trained autoregressive operators (Theorem 6.7).

**(4) TBPTT gradient analysis.** We formalize  $K$ -step truncated backpropagation through time (TBPTT) as a biased stochastic gradient estimator for the autoregressive objective. We prove the cross-window gradient contributions decay geometrically as  $\mathcal{O}(\rho^K)$  (Theorem 7.3), derive the optimal window size  $K^* = \mathcal{O}(\log(T/\sigma^2))$  from a bias-variance decomposition (Corollary 7.4), and establish a non-asymptotic convergence rate for TBPTT-trained autoregressive operators under the Adam optimizer of the form  $\mathcal{O}(1/\sqrt{t}) + \mathcal{O}(\rho^{K^*})$  (Proposition 7.5). Crucially, PINO training and TBPTT form a self-reinforcing cycle: physics constraints reduce  $\rho$ , which shrinks the TBPTT bias

---

<sup>\*1</sup> NVIDIA Corporation.

\* Corresponding author: cetiesam@nvidia.com

**Keywords:** Physics-Informed Neural Operators; Fourier Neural Operators; Sequential Auto-regressive Modeling; Reservoir Simulation; Supervised learning.

for any fixed  $K$ , allowing shorter windows, more gradient steps per epoch, and further physics improvement.

Empirical validation on the full Norne production timeline confirms all theoretical predictions quantitatively. Autoregressive PINO surrogates sustain  $R^2 > 0.99$  (oil saturation),  $R^2 > 0.90$  (gas saturation),  $R^2 \approx 0.80$  (pressure), and monotonically improving  $R^2$  (water saturation) across the full 3298-day horizon, trained on eight NVIDIA B200 (HGX B200 / Blackwell) GPUs in under one hour. In contrast, teacher-forced one-step models degrade to  $R^2 \approx 0.96, 0.38, 0.72,$  and  $0.75$  respectively—with the gas saturation collapse at  $t \approx 1250$  days accurately predicted by the rollout bound of Theorem 5.1 using  $L^G \approx 1.15$  and  $\varepsilon \approx 3 \times 10^{-3}$ . A 1000-member ensemble runs in under one minute on a single NVIDIA B200 GPU, providing a  $\sim 10^4 \times$  wall-clock speedup over the OPM finite-volume simulator and enabling Bayesian inversion and uncertainty quantification workflows at industrial scale.

# 1 Introduction

## 1.1 Motivation

Multiphase flow simulation in heterogeneous porous media is the governing forward problem in petroleum reservoir management, geological carbon storage, and groundwater remediation. Industrial-grade simulators — Newton-Raphson-based implicit finite-volume codes such as the Open Porous Media Flow simulator (OPM) [25] — solve large-scale coupled systems of nonlinear algebraic equations at each timestep, with wall-clock times of hours to days on CPU clusters. In ensemble-based workflows such as history matching, uncertainty quantification (UQ), and production optimization, this single forward solve must be repeated  $10^3$ – $10^5$  times, making direct simulator use computationally prohibitive [10, 11].

Neural-operator surrogates that learn to approximate the simulator response at a fraction of the cost are therefore of substantial practical importance [13, 16, 20, 22]. Among available architectures, the Fourier Neural Operator (FNO) [20] has emerged as a leading approach: it is resolution-invariant by construction (parameters are discretization-independent), provides an efficient global receptive field via spectral convolution, and admits a rigorous universal approximation theory for maps between Banach spaces [16, 19]. Its physics-informed extension PINO [21] additionally penalizes PDE or discrete residuals during training, providing regularization that improves physical consistency.

## 1.2 The sequential surrogate problem and its mathematical challenges

A fundamental difficulty, underappreciated in much of the existing surrogate literature, is that neural operators for reservoir simulation must be deployed *autoregressively*: at each production timestep, predictions are fed back as inputs for subsequent timesteps. This creates a sharp tension between the one-step (teacher-forced, “1–1”) training paradigm — in which ground-truth simulator states are provided at every step — and the closed-loop inference mode in which the model operates. The mismatch is known as *exposure bias* or *covariate shift* in the sequence modeling literature [4, 18, 31] and has been studied in recurrent language models, learned weather forecasters [5, 17, 27], and neural PDE surrogates [36].

The mathematical mechanism underlying this instability is well understood in the theory of iterated function systems and discrete-time dynamical systems. For a learned one-step operator  $\mathcal{G}_\theta$ , the rollout error after  $n$  steps satisfies a recursion driven by the Jacobian product  $\prod_{j=0}^{n-1} D_x \mathcal{G}_\theta(x_j)$  along the predicted trajectory. Even a marginally super-unitary operator norm leads to exponential error amplification [3, 23, 26]. For black-oil reservoirs, the saturation equations are advection-dominated and can develop sharp saturation fronts, gravity fingers, and dissolution-driven instabilities — all of which correspond to Jacobian norms exceeding unity along front-aligned state directions. This makes long-horizon stability a particularly acute concern for gas saturation dynamics in Norne-type systems.

## 1.3 Overview of contributions

The contributions of this paper are organized as follows.

- (i) **Rigorous formulation** (Section 2). We embed the discrete-time black-oil system in a product-Sobolev-space framework. We prove well-posedness of the implicit timestep map, provide sharp local Lipschitz estimates linking the Lipschitz constant to the coercivity of the finite-volume residual, and characterize the elliptic–hyperbolic structural distinction that governs different stability behaviors across state variables.
- (ii) **Covariate shift quantification** (Section 4). We prove explicit  $W_2$  and total-variation bounds on the distributional discrepancy between 1–1 and AR training measures, show this gap drives an exponential population-risk discrepancy for  $L > 1$ , and prove a matching lower bound showing the upper bound is tight for hyperbolic transport.
- (iii) **Rollout error analysis with sharp constants** (Section 5). We prove a sharp rollout bound covering general, uniform, contractive, and marginally unstable cases, together with a characterization of which PDE types fall in each regime. A dimension-dependent amplification factor is derived for the mixed-elliptic–hyperbolic Norne state space.
- (iv) **PINO spectral stability theory** (Section 6). We prove that PINO training constrains the learned Jacobian spectral radius below the true dissipation rate, with explicit constants. We show the physics residual acts as a spectral Jacobian regularizer and prove a uniform-in-time PINO rollout bound.
- (v) **TBPTT gradient bias theory** (Section 7). Full bias-variance analysis of  $K$ -step TBPTT as a gradient estimator, including optimal window size selection and a convergence rate under Adam.

- (vi) **FNO approximation theory for mixed PDE types** (Section 8). We prove spectral approximation rates for FNO applied to elliptic versus hyperbolic variables and quantify why gas saturation requires deeper networks or AR training to compensate for Gibbs-like spectral truncation artifacts near fronts.
- (vii) **Empirical validation on Norne** (Section 11). Full time-resolved  $R^2$  benchmarks for all four state variables, with theory-consistent quantitative interpretation of each observed behavior.

## 2 Mathematical Preliminaries

### 2.1 Domains, grids, and function spaces

Let  $\Omega \subset \mathbb{R}^3$  be an open bounded Lipschitz domain representing the reservoir. We work with the Norne Cartesian grid of dimensions  $(n_x, n_y, n_z) = (46, 112, 22)$ , yielding  $N := n_x n_y n_z = 113,344$  cells. Each cell  $\Omega_i \subset \Omega$  is a rectangular cuboid of volume  $|\Omega_i| > 0$ . For  $1 \leq p \leq \infty$ ,  $L^p(\Omega)$  is the standard Lebesgue space;  $H^s(\Omega)$  the Sobolev space of order  $s \geq 0$ . On the discrete grid, a scalar field  $a : \Omega \rightarrow \mathbb{R}$  sampled cell-wise is identified with a vector  $a \in \mathbb{R}^N$ . The discrete  $\ell^p$  norm is  $\|a\|_p := (\sum_i |a_i|^p)^{1/p}$  and the grid  $L^p$  norm (with cell volumes) is

$$\|a\|_{L_h^p} := \left( \sum_{i=1}^N |\Omega_i| |a_i|^p \right)^{1/p}.$$

**Definition 2.1** (Pore-volume weighted inner product). *Define the pore-volume-weighted inner product on  $\mathbb{R}^N$ :*

$$\langle a, b \rangle_\phi := \sum_{i=1}^N \phi_i |\Omega_i| a_i b_i,$$

where  $\phi_i \in (0, 1)$  is the cell porosity. The induced norm  $\|a\|_\phi := \sqrt{\langle a, a \rangle_\phi}$  weights errors proportionally to pore volume, which is the physically natural metric for mass-conservation-relevant quantities.

### 2.2 The black-oil PDE system and its structure

The three-phase (water, oil, gas) black-oil model on  $\Omega \times (0, T_f]$  is:

$$\phi \frac{\partial S_w}{\partial t} - \nabla \cdot [T_w (\nabla P_w + \rho_w g \mathbf{e}_3)] = Q_w, \quad (1)$$

$$\phi \frac{\partial S_o}{\partial t} - \nabla \cdot [T_o (\nabla P_o + \rho_o g \mathbf{e}_3)] = Q_o, \quad (2)$$

$$\frac{\partial}{\partial t} \left[ \phi \left( \frac{\rho_g}{B_g} S_g + \frac{R_{so} \rho_g}{B_o} S_o \right) \right] - \nabla \cdot \left[ \frac{\rho_g}{B_g} T_g (\nabla P_g + \rho_g g \mathbf{e}_3) \right. \quad (3)$$

$$\left. + \frac{R_{so} \rho_g}{B_o} T_o (\nabla P_o + \rho_o g \mathbf{e}_3) \right] = Q_g. \quad (4)$$

with saturation constraint  $S_w + S_o + S_g = 1$  and capillary relations  $P_{cwo} := P_o - P_w$ ,  $P_{cog} := P_g - P_o$ . The phase transmissibilities are

$$T_\alpha := \frac{K(x) K_{r\alpha}(S)}{\mu_\alpha}, \quad \alpha \in \{w, o, g\}, \quad (5)$$

where  $K(x) > 0$  is the absolute permeability tensor (treated as scalar here),  $K_{r\alpha} \geq 0$  are relative permeability functions, and  $\mu_\alpha > 0$  are phase viscosities. When a fault transmissibility multiplier (FTM)  $f \in [0, 1]$  is present,  $K$  is replaced by  $f \cdot K$ . The boundary condition is  $\nabla P_\alpha \cdot \nu = 0$  on  $\partial\Omega$  (no-flow).

**Elliptic-hyperbolic structure.** After summing equations (1)–(4) with appropriate formation-volume-factor weights, the total compressibility equation for pressure takes the form

$$-\nabla \cdot [T_{\text{tot}} \nabla P] + c_t \phi \frac{\partial P}{\partial t} = Q_{\text{tot}}, \quad T_{\text{tot}} := T_w + T_o + T_g, \quad (6)$$

which is a parabolic (nearly elliptic for small  $c_t$ ) equation for pressure. Substituting the Darcy flux into the saturation equations gives a nonlinear advection-diffusion system for  $S_w, S_o, S_g$  with characteristic speed  $v_\alpha = T_\alpha / \phi$ , which is hyperbolic-dominated for typical mobility ratios. For gas, the combination of free gas ( $B_g^{-1} S_g$ ) and dissolved gas ( $R_{so} B_o^{-1} S_o$ ) makes the gas equation strongly nonlinear and particularly sensitive to front tracking.

### 2.3 Discrete-time formulation and state space

**Definition 2.2** (State space). *The physically admissible state space is*

$$\mathcal{X} := \{x = (p, S_w, S_o, S_g) \in \mathbb{R}^{4N} \mid p_i > 0, S_{\alpha,i} \geq 0 \forall \alpha, i, S_{w,i} + S_{o,i} + S_{g,i} = 1 \forall i\}.$$

The constraint  $S_w + S_o + S_g = \mathbf{1}_N$  defines a hyperplane in  $\mathbb{R}^{3N}$ ; thus  $\mathcal{X}$  is a closed convex subset of  $\mathbb{R}^{4N}$  of intrinsic dimension  $3N + 1$  (pressure has  $N$  degrees of freedom; saturations have  $2N$  after the volume constraint).

**Definition 2.3** (Input channels). *Static reservoir parameters:  $u := (\log k, \phi, f) \in \mathbb{R}^{3N}$ . Well controls at step  $n$ :  $c_n := (Q_n, Q_{w,n}, Q_{g,n}) \in \mathbb{R}^{3N_w}$ ,  $N_w = 22$  producers + 13 injectors. Temporal scalars:  $\tau_n := (t_n, \Delta t_n) \in \mathbb{R}^2$ . The full input at step  $n$  is  $\xi_n := (u, x_n, c_n, \tau_n)$ .*

### 2.4 The finite-volume residual operator and well-posedness

The implicit (backward-Euler) finite-volume discretization of (1)–(4) at timestep  $n \rightarrow n + 1$  assembles the nonlinear algebraic system

$$R(x_{n+1}, x_n; u, c_n, \tau_n) = 0, \quad (7)$$

where  $R : \mathbb{R}^{4N} \times \mathbb{R}^{4N} \times \mathbb{R}^{3N} \times \mathbb{R}^{3N_w} \times \mathbb{R}^2 \rightarrow \mathbb{R}^{4N}$  is the *finite-volume residual operator*. Its water-component block at cell  $i$  reads explicitly:

$$R_i^w(x^+, x^-) := \phi_i \frac{S_{w,i}^+ - S_{w,i}^-}{\Delta t} - \sum_{j \in \mathcal{N}(i)} \frac{T_w^{ij,+}}{d_{ij}} (P_{w,j}^+ - P_{w,i}^+) |\partial \Omega_{ij}| - Q_{w,i}, \quad (8)$$

where  $x^+ = x_{n+1}$ ,  $x^- = x_n$ ,  $\mathcal{N}(i)$  is the cell-face stencil,  $T_w^{ij,+}$  is the upstream-weighted transmissibility at face  $ij$  evaluated at the new state, and  $d_{ij}$  is the cell-center distance. Analogous blocks  $R_i^o$  and  $R_i^g$  are defined for oil and gas, with the gas block including the formation-volume-factor-weighted accumulation term  $\phi_i \Delta t^{-1} [(\rho_g/B_g) S_{g,i}^+ + (R_{so} \rho_g/B_o) S_{o,i}^+ - (\rho_g/B_g) S_{g,i}^- - (R_{so} \rho_g/B_o) S_{o,i}^-]$ .

**Assumption 2.4** (Discrete coercivity). *For all  $x^- \in \mathcal{X}$  and all  $\Delta t \in (0, \Delta t_{\max}]$ , the Jacobian of  $R$  with respect to its first argument evaluated at any  $(x^+, x^-) \in \mathcal{X}^2$  satisfies a coercivity condition:*

$$\left\langle \frac{\partial R}{\partial x^+}(x^+, x^-) v, v \right\rangle_{\phi^{-1}} \geq \alpha \|v\|_{\phi}^2 \quad \forall v \in \mathbb{R}^{4N}, \quad (9)$$

for some  $\alpha > 0$  depending on  $\Delta t_{\max}$ ,  $\min \phi_i$ ,  $\min K_i$ , the relative permeability slopes, and the capillary pressure derivatives.

**Remark 2.5.** *Assumption 2.4 holds for the standard implicit finite-volume scheme when capillary pressure  $P_{c,\alpha}(S)$  is monotone (which is physical) and  $\Delta t$  is below a threshold determined by the stability of the advective flux linearization. The coercivity constant  $\alpha$  is bounded below by  $\alpha \geq \phi_{\min}/\Delta t_{\max} - C_{\text{adv}}$ , where  $C_{\text{adv}}$  is related to the maximum phase velocity.*

**Theorem 2.6** (Well-posedness of the implicit timestep). *Under Assumption 2.4, for each  $x_n \in \mathcal{X}$ ,  $u \in \mathbb{R}^{3N}$ ,  $c_n \in \mathbb{R}^{3N_w}$ , and  $\tau_n$  with  $0 < \Delta t_n \leq \Delta t_{\max}$ , there exists a unique solution  $x_{n+1} \in \mathcal{X}$  to (7). This defines the true time-advance map  $\mathcal{F} : \mathcal{X} \rightarrow \mathcal{X}$  by*

$$\mathcal{F}(x_n; u, c_n, \tau_n) := x_{n+1}. \quad (10)$$

*Proof.* Define  $\Psi_{x^-}(x^+) := x^+ - \alpha^{-1} (\partial R/\partial x^+)^{-1} R(x^+, x^-; \cdot)$  restricted to  $\mathcal{X}$ . Coercivity (9) implies  $\partial R/\partial x^+$  is invertible with  $\|(\partial R/\partial x^+)^{-1}\|_{\phi^{-1} \rightarrow \phi} \leq \alpha^{-1}$ . A contraction estimate shows  $\Psi_{x^-}$  maps a closed ball  $B_r(x^-)$  to itself for sufficiently small  $r$  (using the Lipschitz continuity of  $R$  in both arguments), and the Banach fixed-point theorem yields a unique fixed point, which is the solution  $x^+$ . Uniqueness follows immediately from strict monotonicity of  $R$  in  $x^+$ : if  $R(a, x^-) = R(b, x^-) = 0$  with  $a \neq b$ , then  $0 = \langle R(a, x^-) - R(b, x^-), a - b \rangle_{\phi^{-1}} \geq \alpha \|a - b\|_{\phi}^2 > 0$ , a contradiction. The solution lies in  $\mathcal{X}$  by checking that the saturation constraint is preserved under the implicit update (it is, since the residual explicitly includes the volume constraint via the capillary pressure formulation).  $\square$

**Lemma 2.7** (Local Lipschitz estimate for  $\mathcal{F}$ ). *Under Assumption 2.4, for any  $x, y \in \mathcal{X}$  with  $\|x - y\|_{\phi} \leq r$ :*

$$\|\mathcal{F}(x; \cdot) - \mathcal{F}(y; \cdot)\|_{\phi} \leq L_{\mathcal{F}}(r) \|x - y\|_{\phi}, \quad (11)$$

where

$$L_{\mathcal{F}}(r) = 1 + \frac{\|\partial R/\partial x^-\|_{\phi}}{\alpha} \leq 1 + \frac{C_{\text{flux}}(r)}{\alpha}, \quad (12)$$

and  $C_{\text{flux}}(r)$  captures the inter-cell flux Jacobian magnitude. For the pressure component alone (elliptic),  $L_{\mathcal{F}}^P \leq 1 + C_{\text{ell}}/\alpha$  with  $C_{\text{ell}}$  depending on  $T_{\text{tot}}$ . For the gas saturation component (hyperbolic),  $L_{\mathcal{F}}^G$  can exceed unity by an amount proportional to the local front velocity.

*Proof.* Let  $x_x^+ := \mathcal{F}(x; \cdot)$  and  $x_y^+ := \mathcal{F}(y; \cdot)$ . Then  $R(x_x^+, x; \cdot) = R(x_y^+, y; \cdot) = 0$ . Subtracting and applying the mean-value theorem:

$$\frac{\partial R}{\partial x^+} \Big|_{\xi} \cdot (x_x^+ - x_y^+) = -\frac{\partial R}{\partial x^-} \Big|_{\eta} \cdot (x - y),$$

where  $\xi$  and  $\eta$  lie on the line segment. Inverting with the coercivity bound:

$$\|x_x^+ - x_y^+\|_{\phi} \leq \frac{1}{\alpha} \left\| \frac{\partial R}{\partial x^-} \Big|_{\eta} \right\|_{\phi \rightarrow \phi} \|x - y\|_{\phi} =: \frac{C_{\text{flux}}(r)}{\alpha} \|x - y\|_{\phi}.$$

For the pressure block,  $\partial R^P / \partial x^-$  is dominated by the accumulation term  $\phi / \Delta t$ , and  $C_{\text{ell}} \approx \phi_{\text{max}} / \Delta t$ . For gas, the off-diagonal coupling through relative permeability nonlinearities adds terms proportional to front velocities, giving the larger  $C_{\text{flux}}^G$ .  $\square$

## 2.5 Neural operator surrogate and rollout

**Definition 2.8** (Learned one-step operator). *A neural operator surrogate is a parametric family  $\{\mathcal{G}_{\theta} : \theta \in \Theta \subset \mathbb{R}^P\}$  of maps  $\mathcal{G}_{\theta} : \mathcal{X} \times \mathbb{R}^{3N} \times \mathbb{R}^{3N_w} \times \mathbb{R}^2 \rightarrow \mathcal{X}$  approximating  $\mathcal{F}$ . For FNO, the architecture is described in Section 8.*

**Definition 2.9** (Autoregressive rollout). *Given initial condition  $x_0 \in \mathcal{X}$ , define the closed-loop trajectory*

$$\hat{x}_0 := x_0, \quad \hat{x}_{n+1} := \mathcal{G}_{\theta}(u, \hat{x}_n, c_n, \tau_n), \quad n = 0, \dots, T-1. \quad (13)$$

The  $n$ -step rollout operator is the composition

$$\mathcal{G}_{\theta}^{(n)}(x_0) := \underbrace{\mathcal{G}_{\theta} \circ \dots \circ \mathcal{G}_{\theta}}_n(x_0). \quad (14)$$

The rollout error at step  $n$  is  $\delta_n := \hat{x}_n - x_n$ .

## 2.6 Probability spaces and distributional setup

Let  $(\Omega_{\omega}, \mathcal{A}, \mathbb{P})$  be a probability space supporting random initial conditions  $x_0 \sim \mu_0$ , static fields  $u$ , and control sequences  $c_{0:T-1}$ . Define:

$$\begin{aligned} \mu_n &:= \text{law}(x_n) \quad \text{under true simulator trajectories,} \\ \hat{\mu}_n^{\theta} &:= \text{law}(\hat{x}_n) \quad \text{under AR rollout (13).} \end{aligned}$$

The empirical training measure on one-step pairs from  $N_s$  simulator trajectories is

$$\hat{\mathbb{P}}_N := \frac{1}{N_s T} \sum_{i=1}^{N_s} \sum_{n=0}^{T-1} \delta_{(x_n^{(i)}, x_{n+1}^{(i)}, \xi_n^{(i)})}.$$

**Remark 2.10** (The covariate shift problem, precisely stated). *The 1–1 empirical risk minimizer  $\hat{\theta}^{1-1}$  minimizes  $\mathbb{E}_{\hat{\mathbb{P}}_N}[\ell(\mathcal{G}_{\theta}(\xi_n), x_{n+1})]$ , i.e., the loss is evaluated at inputs drawn from  $\mu_n$  (the true state distribution). At deployment, the surrogate is evaluated at inputs drawn from  $\hat{\mu}_n^{\theta}$  (the predicted state distribution). Whenever  $\hat{\mu}_n^{\theta} \neq \mu_n$ , the model operates outside its training distribution, and its actual deployment error can be far larger than the training loss suggests. The magnitude of this gap is the subject of Section 4.*

## 3 Two Training Paradigms and Risk Analysis

### 3.1 One-step (teacher-forced) training

**Definition 3.1** (1–1 loss). *The one-step (teacher-forced) population risk is*

$$\mathcal{L}_{1-1}(\theta) := \mathbb{E} \left[ \frac{1}{T} \sum_{n=0}^{T-1} \ell(\mathcal{G}_{\theta}(\xi_n), x_{n+1}) \right], \quad (15)$$

where  $\xi_n = (u, x_n, c_n, \tau_n)$  with  $x_n$  drawn from  $\mu_n$ , and  $\ell(a, b) := \|a - b\|_\phi^2 / \|b\|_\phi^2$  is the relative  $\ell^2$  loss. The empirical version over  $N_s$  trajectories is

$$\hat{\mathcal{L}}_{1-1}(\theta) = \frac{1}{N_s T} \sum_{i=1}^{N_s} \sum_{n=0}^{T-1} \ell(\mathcal{G}_\theta(\xi_n^{(i)}), x_{n+1}^{(i)}). \quad (16)$$

### 3.2 Autoregressive (closed-loop) training

**Definition 3.2** (AR loss). *The autoregressive population risk is*

$$\mathcal{L}_{\text{AR}}(\theta) := \mathbb{E} \left[ \frac{1}{T} \sum_{n=0}^{T-1} \ell(\hat{x}_{n+1}(\theta), x_{n+1}) \right], \quad (17)$$

where  $\hat{x}_n(\theta)$  is the AR rollout (13). The expectation is over  $(x_0, u, c_{0:T-1}) \sim \mathbb{P}$ .

**Remark 3.3** (Gradient structure of AR loss). *The gradient of  $\mathcal{L}_{\text{AR}}$  with respect to  $\theta$  is*

$$\nabla_\theta \mathcal{L}_{\text{AR}}(\theta) = \frac{1}{T} \sum_{n=0}^{T-1} \sum_{m=0}^n \mathbb{E} \left[ \frac{\partial \ell(\hat{x}_{n+1}, x_{n+1})}{\partial \hat{x}_{n+1}} \underbrace{\left( \prod_{j=m+1}^n D_x \mathcal{G}_\theta(\hat{\xi}_j) \right)}_{\text{Jacobian chain}} D_\theta \mathcal{G}_\theta(\hat{\xi}_m) \right], \quad (18)$$

where  $\hat{\xi}_j := (u, \hat{x}_j, c_j, \tau_j)$ . The Jacobian chain  $\prod_{j=m+1}^n D_x \mathcal{G}_\theta(\hat{\xi}_j) \in \mathbb{R}^{4N \times 4N}$  is the product of  $n - m$  matrices, which can explode for  $\|D_x \mathcal{G}_\theta\|_{\text{op}} > 1$  or vanish for  $\|D_x \mathcal{G}_\theta\|_{\text{op}} < 1$ . This is the central numerical challenge motivating TBPTT.

### 3.3 Generalization bounds

**Theorem 3.4** (Uniform generalization bound). *Let  $\mathcal{H} = \{\mathcal{G}_\theta : \theta \in \Theta\}$  be the hypothesis class,  $\ell$  be  $L_\ell$ -Lipschitz in its first argument and bounded by  $M_\ell > 0$ . With probability  $\geq 1 - \delta$  over the draw of  $N_s$  i.i.d. trajectories,*

$$\sup_{\theta \in \Theta} |\mathcal{L}_{1-1}(\theta) - \hat{\mathcal{L}}_{1-1}(\theta)| \leq 2L_\ell \mathfrak{R}_{N_s}(\mathcal{H}) + M_\ell \sqrt{\frac{\log(1/\delta)}{2N_s}}, \quad (19)$$

where  $\mathfrak{R}_{N_s}(\mathcal{H})$  is the Rademacher complexity of  $\mathcal{H}$  with respect to  $\hat{\mathbb{P}}_{N_s}$ .

*Proof.* Define the composed function class  $\mathcal{F}_{\mathcal{H}} := \{(a, b) \mapsto \ell(\mathcal{G}_\theta(a), b) : \theta \in \Theta\}$ . Since  $\ell$  is  $L_\ell$ -Lipschitz, the Rademacher contraction lemma (Ledoux–Talagrand) gives  $\mathfrak{R}_{N_s}(\mathcal{F}_{\mathcal{H}}) \leq L_\ell \mathfrak{R}_{N_s}(\mathcal{H})$ . The uniform bound (19) then follows from the standard symmetric Rademacher argument applied to the function  $(d_1, \dots, d_{N_s}) \mapsto \sup_\theta |\mathcal{L} - \hat{\mathcal{L}}|$ , combined with McDiarmid’s inequality (bounded differences of size  $2M_\ell/N_s$ ) and symmetrization via Rademacher variables [2].  $\square$

**Proposition 3.5** (Physics constraints reduce Rademacher complexity). *Let  $\Theta_{\text{phys}}(\lambda) \subset \Theta$  denote the sublevel set  $\{\theta : \mathbb{E}[\|R(\mathcal{G}_\theta(\xi_n), x_n; \cdot)\|^2] \leq 1/\lambda\}$ . Then  $\mathfrak{R}_{N_s}(\mathcal{H}_{\text{phys}}) \leq \mathfrak{R}_{N_s}(\mathcal{H})$ , with equality only if the physics penalty is non-binding. Moreover, for FNO hypothesis classes parameterized by spectral mode coefficients  $\{R^{(\ell)}(k)\}$ , the PINO physics constraint reduces the effective covering number:*

$$\log \mathcal{N}(\mathcal{H}_{\text{phys}}, \varepsilon, \|\cdot\|_\infty) \leq \log \mathcal{N}(\mathcal{H}, \varepsilon, \|\cdot\|_\infty) - C\lambda^{1/2} \varepsilon^{-d_{\text{phys}}}, \quad (20)$$

where  $d_{\text{phys}} > 0$  is the effective co-dimension of  $\mathcal{M}$  in  $\mathcal{X}$  and  $C$  depends on the coercivity constant  $\alpha$  in Assumption 2.4.

*Proof.*  $\mathcal{H}_{\text{phys}} \subset \mathcal{H}$  implies the first claim by monotonicity of Rademacher complexity in the function class. For the covering number bound, note that the physics constraint  $\mathbb{E}[\|R(\mathcal{G}_\theta, x_n; \cdot)\|^2] \leq 1/\lambda$  restricts  $\mathcal{G}_\theta$  to lie within an  $\mathcal{O}(\lambda^{-1/2})$ -tube of the manifold  $\mathcal{M}$  in the  $L^2(\mathbb{P}_X)$ -sense. Standard metric entropy estimates for tube neighborhoods of smooth manifolds of co-dimension  $d$  give the  $\varepsilon^{-d_{\text{phys}}}$  correction.  $\square$

## 4 Covariate Shift: Quantitative Analysis

### 4.1 Wasserstein and total-variation bounds

**Theorem 4.1** (Covariate shift quantification). *Assume  $\mathcal{G}_\theta$  has Lipschitz constant  $L \geq 0$  (in the  $\|\cdot\|_\phi$  metric) and one-step error bounded by  $\varepsilon > 0$ :*

$$\|\mathcal{G}_\theta(u, x, c, \tau) - \mathcal{F}(x; u, c, \tau)\|_\phi \leq \varepsilon \quad \forall x \in \mathcal{X}.$$

Then, for every  $n \geq 1$ :

(a) Wasserstein-2 bound:

$$W_2(\hat{\mu}_n^\theta, \mu_n) \leq \varepsilon \frac{L^n - 1}{L - 1} \quad (L \neq 1), \quad W_2(\hat{\mu}_n^\theta, \mu_n) \leq n\varepsilon \quad (L = 1). \quad (21)$$

(b) Contractive case: For  $L < 1$ ,

$$W_2(\hat{\mu}_n^\theta, \mu_n) \leq \frac{\varepsilon}{1 - L} \quad \forall n \geq 0. \quad (22)$$

(c) Risk discrepancy: For any  $L_\ell$ -Lipschitz loss  $\ell$ ,

$$|\mathbb{E}_{\mu_n}[\ell(\mathcal{G}_\theta, \cdot)] - \mathbb{E}_{\hat{\mu}_n^\theta}[\ell(\mathcal{G}_\theta, \cdot)]| \leq L_\ell W_2(\hat{\mu}_n^\theta, \mu_n). \quad (23)$$

(d) Total population-risk gap:

$$|\mathcal{L}_{1-1}(\theta) - \mathcal{L}_{\text{AR}}(\theta)| \leq \frac{L_\ell \varepsilon}{T} \sum_{n=0}^{T-1} \frac{L^n - 1}{L - 1} = \frac{L_\ell \varepsilon}{T} \cdot \frac{L^T - TL + T - 1}{(L - 1)^2}. \quad (24)$$

*Proof.* Part (a). Construct the canonical coupling  $(\hat{x}_n, x_n)$  by running both the predicted and true trajectories from the same initial condition  $x_0$ :

$$\hat{x}_{n+1} = \mathcal{G}_\theta(u, \hat{x}_n, c_n, \tau_n), \quad x_{n+1} = \mathcal{F}(x_n; u, c_n, \tau_n).$$

Define  $\delta_n := \hat{x}_n - x_n$  with  $\delta_0 = 0$ . Adding and subtracting  $\mathcal{G}_\theta(u, x_n, c_n, \tau_n)$ :

$$\begin{aligned} \|\delta_{n+1}\|_\phi &= \|\mathcal{G}_\theta(u, \hat{x}_n, c_n, \tau_n) - \mathcal{F}(x_n; u, c_n, \tau_n)\|_\phi \\ &\leq \|\mathcal{G}_\theta(u, \hat{x}_n, \cdot) - \mathcal{G}_\theta(u, x_n, \cdot)\|_\phi + \|\mathcal{G}_\theta(u, x_n, \cdot) - \mathcal{F}(x_n; \cdot)\|_\phi \\ &\leq L \|\delta_n\|_\phi + \varepsilon. \end{aligned}$$

Iterating from  $\delta_0 = 0$ :  $\|\delta_n\|_\phi \leq \sum_{j=0}^{n-1} L^{n-1-j} \varepsilon = \varepsilon(L^n - 1)/(L - 1)$  for  $L \neq 1$ . Since the Wasserstein-2 distance satisfies  $W_2(\hat{\mu}_n^\theta, \mu_n)^2 \leq \mathbb{E}[\|\hat{x}_n - x_n\|_\phi^2] \leq \|\delta_n\|_\phi^2$  (using the constructed coupling as a transport plan), and the pathwise bound  $\|\delta_n\|_\phi \leq \varepsilon(L^n - 1)/(L - 1)$  holds for all  $\omega$  in the probability space, taking the square root gives (21).

Part (b). For  $L < 1$ , the geometric series gives  $\sum_{j=0}^{n-1} L^{n-1-j} \leq 1/(1 - L)$  independent of  $n$ .

Part (c). For any  $L_\ell$ -Lipschitz function  $g$ , the dual representation of the Wasserstein-1 distance gives  $|\mathbb{E}_{\mu} g - \mathbb{E}_{\nu} g| \leq L_g W_1(\mu, \nu) \leq L_g W_2(\mu, \nu)$  (since  $W_1 \leq W_2$  by Cauchy-Schwarz on the transport plan).

Part (d). Apply (c) to each summand in  $\mathcal{L}_{1-1} - \mathcal{L}_{\text{AR}}$  and sum over  $n = 0, \dots, T - 1$ , then divide by  $T$ :

$$|\mathcal{L}_{1-1} - \mathcal{L}_{\text{AR}}| \leq \frac{L_\ell}{T} \sum_{n=0}^{T-1} \frac{\varepsilon(L^n - 1)}{L - 1} = \frac{L_\ell \varepsilon}{T(L - 1)} \left( \frac{L^T - 1}{L - 1} - T \right),$$

which simplifies to (24). □

**Corollary 4.2** (Exponential risk gap for  $L > 1$ ). *If  $L > 1$  and  $\varepsilon > 0$ , then*

$$|\mathcal{L}_{1-1}(\theta) - \mathcal{L}_{\text{AR}}(\theta)| = \Theta\left(\frac{L_\ell \varepsilon L^T}{T(L - 1)^2}\right),$$

*i.e., the population-risk gap grows exponentially in the horizon  $T$ . A model achieving small 1-1 training loss can have arbitrarily large AR deployment loss when  $L > 1$ .*

*Proof.* For large  $T$ , the dominant term in (24) is  $L_\ell \varepsilon L^T / (T(L-1)^2)$ . The  $\Theta$  (i.e., matching upper and lower bounds) follows because the  $n = T - 1$  term alone already contributes  $L_\ell \varepsilon L^{T-1} / ((L-1)T)$ .  $\square$

**Remark 4.3** (Gas saturation vs. pressure in Norne). *For pressure (elliptic),  $L = L^P \approx 1$  (marginally stable), so the risk gap grows as  $O(T\varepsilon)$  — slowly. For gas saturation (hyperbolic front),  $L = L^G > 1$ , so the gap grows exponentially, explaining the catastrophic 1–1 model failure in Figure 2d.*

## 4.2 Lower bound: the bound is sharp for hyperbolic transport

**Proposition 4.4** (Sharpness for hyperbolic transport). *Consider the one-dimensional scalar conservation law  $\partial_t S + v \partial_x S = 0$  on a periodic grid of  $N$  cells, discretized by a first-order upwind scheme with CFL number  $\nu = v \Delta t / \Delta x$ . For  $\nu \in (0, 1)$ , the discrete time-advance operator has  $\|D_x \mathcal{F}\|_{\text{op}, \ell^2} \in [1 - \nu, 1]$  and the bound in Theorem 4.1(a) is tight to within a constant factor: for any  $\theta$  with  $\|\mathcal{G}_\theta - \mathcal{F}\|_\infty = \varepsilon$ , there exists an initial condition  $x_0$  such that*

$$\|\hat{x}_n - x_n\|_{\ell^2} \geq c \varepsilon n$$

for a universal constant  $c > 0$ .

*Proof.* The upwind Jacobian has spectrum  $\{1 - \nu(1 - e^{-ik\Delta x}) : k = 0, \dots, N-1\}$ , giving  $\|D_x \mathcal{F}\|_{\text{op}, \ell^2} = 1$  for  $k = 0$  (the DC mode). For a perturbation  $\varepsilon$  aligned with the DC eigenvector (a constant shift),  $\mathcal{G}_\theta(x) = \mathcal{F}(x) + \varepsilon \mathbf{1}_N$  (constant modeling offset). Then  $\|\hat{x}_n - x_n\|_{\ell^2} = n\varepsilon \|\mathbf{1}_N\|_{\ell^2} = n\varepsilon \sqrt{N}$ , matching the  $L = 1$  bound with  $c = 1/\sqrt{N}$ . For  $L > 1$ , a perturbation aligned with the growing eigenmode (exists when  $\nu > 1$  or near resonance) gives exponential growth.  $\square$

## 5 Rollout Error: Sharp Analysis

### 5.1 The fundamental rollout error recursion

**Theorem 5.1** (Decomposed rollout error bound). *Let  $L \geq 0$  be the Lipschitz constant of  $\mathcal{G}_\theta$  and define the open-loop one-step residual on true states:*

$$e_n := \|\mathcal{G}_\theta(\xi_n) - x_{n+1}\|_\phi. \quad (25)$$

Then for all  $n \geq 1$ :

(a) General bound:

$$\|\delta_n\|_\phi \leq \sum_{j=0}^{n-1} L^{n-1-j} e_j. \quad (26)$$

(b) Uniform error ( $e_j \leq \varepsilon$  for all  $j$ ):

$$\|\delta_n\|_\phi \leq \varepsilon \frac{L^n - 1}{L - 1} \quad (L \neq 1), \quad \|\delta_n\|_\phi \leq n\varepsilon \quad (L = 1). \quad (27)$$

(c) Contractive case ( $L < 1$ ):

$$\|\delta_n\|_\phi \leq \frac{\varepsilon}{1 - L}, \quad \forall n \geq 0. \quad (28)$$

(d) Marginally unstable case ( $L = 1 + \eta$ ,  $0 < \eta \ll 1$ ):

$$\|\delta_n\|_\phi \leq \varepsilon \frac{e^{\eta n} - 1}{\eta} \leq \frac{\varepsilon n e^{\eta n}}{\eta n} = \varepsilon n e^{\eta n}. \quad (29)$$

*Proof.* Part (a). Add and subtract  $\mathcal{G}_\theta(\xi_n)$  evaluated at the true state:

$$\begin{aligned} \|\delta_{n+1}\|_\phi &= \|\mathcal{G}_\theta(u, \hat{x}_n, c_n, \tau_n) - x_{n+1}\|_\phi \\ &\leq \|\mathcal{G}_\theta(u, \hat{x}_n, c_n, \tau_n) - \mathcal{G}_\theta(u, x_n, c_n, \tau_n)\|_\phi + \|\mathcal{G}_\theta(u, x_n, c_n, \tau_n) - x_{n+1}\|_\phi \\ &\leq L \|\delta_n\|_\phi + e_n. \end{aligned}$$

This is the fundamental recursion  $\|\delta_{n+1}\|_\phi \leq L \|\delta_n\|_\phi + e_n$ . With  $\delta_0 = 0$ , unrolling gives (26):  $\|\delta_n\|_\phi \leq \sum_{j=0}^{n-1} L^{n-1-j} e_j$ .

Part (b). Set  $e_j = \varepsilon$  and sum the geometric series:  $\|\delta_n\|_\phi \leq \varepsilon \sum_{j=0}^{n-1} L^{n-1-j} = \varepsilon(L^n - 1)/(L - 1)$ .

Part (c). For  $L < 1$ ,  $\|\delta_n\|_\phi \leq \varepsilon \sum_{k=0}^{n-1} L^k \leq \varepsilon/(1 - L)$ .

Part (d). For  $L = 1 + \eta$ ,  $(1 + \eta)^n \leq e^{\eta n}$  (Bernoulli inequality in reverse), so  $\varepsilon(L^n - 1)/(L - 1) \leq \varepsilon(e^{\eta n} - 1)/\eta \leq \varepsilon n e^{\eta n}$ .  $\square$

**Theorem 5.2** (Dimension-dependent amplification in mixed-type systems). *For the Norne system with state  $x = (p, S_w, S_o, S_g) \in \mathbb{R}^{4N}$ , write  $\delta_n = (\delta_n^P, \delta_n^W, \delta_n^O, \delta_n^G)$  for the component errors. Assume  $D_x \mathcal{F}$  has block structure reflecting the elliptic–hyperbolic coupling, with blocks  $A^{PP}, A^{PS}, A^{SP}, A^{SS}$  (pressure–pressure, pressure–saturation, saturation–pressure, saturation–saturation). Then:*

(a) *The pressure error satisfies*

$$\|\delta_n^P\|_\phi \leq (L^P)^n \|\delta_0^P\|_\phi + \sum_{j=0}^{n-1} (L^P)^{n-1-j} (e_j^P + C_{PS} \|\delta_j^S\|_\phi), \quad (30)$$

where  $L^P \leq 1 + \mathcal{O}((\Delta t)^{-1} \alpha^{-1})$  is close to (or below) unity due to elliptic regularization, and  $C_{PS}$  captures saturation-to-pressure coupling.

(b) *The gas saturation error can grow faster than the overall system Lipschitz constant suggests:*

$$\|\delta_n^G\|_\phi \geq c_G \varepsilon^G \frac{(L^G)^n - 1}{L^G - 1} \quad (31)$$

for some  $L^G > L^P$  when the mobility ratio  $M := K_{rg}/(\mu_g K_{ro}/\mu_o) > 1$  (favorable displacement unstable), which is typical in Norne-type gas injection scenarios.

*Proof sketch.* Part (a): The pressure block  $R^P$  is governed by the pressure equation (6). The implicit Jacobian block  $(\partial R^P / \partial p^+)^{-1}$  is bounded above in operator norm by  $C_{\text{ell}}$  (a fixed multiple of  $T_{\text{tot}}$ -related constants) due to elliptic coercivity of the pressure operator. This gives  $L^P < 1$  or  $L^P \approx 1$ , resulting in controlled error accumulation. The coupling term  $C_{PS} \|\delta_j^S\|$  accounts for saturation changes feeding back into the pressure equation through the total mobility  $T_{\text{tot}}$ .

Part (b): The gas saturation block  $R^G$  includes the nonlinear relative permeability  $K_{rg}(S_g)$  and the dissolved gas coupling. For  $M > 1$ , the gas front advances faster than stable displacement, and small perturbations in  $S_g$  near the front are amplified by the characteristic speed mismatch. A first-order WKB analysis of the linearized transport equation near the front shows an effective amplification factor  $L^G = L^G(\text{front velocity}) > 1$ . The lower bound (31) follows by constructing an explicit perturbation aligned with the unstable front mode.  $\square$

## 5.2 The AR training advantage: Lipschitz constant reduction on the predicted manifold

**Assumption 5.3** (AR contractivity on predicted manifold). *Under autoregressive training with loss  $\mathcal{L}_{\text{AR}}$ , the effective Lipschitz constant of  $\mathcal{G}_\theta$  on the predicted-state distribution  $\hat{\mu}_n^\theta$  satisfies*

$$\tilde{L} := \sup_n \mathbb{E}_{\hat{x} \sim \hat{\mu}_n^\theta} [\|D_x \mathcal{G}_\theta(u, \hat{x}, c, \tau)\|_{\text{op}, \phi}] < L,$$

where  $L$  is the global Lipschitz constant.

**Proposition 5.4** (Stability improvement from AR training). *Under Assumption 5.3, the expected rollout error under AR training satisfies*

$$\mathbb{E} \|\delta_n\|_\phi \leq \tilde{L}^n \mathbb{E} \|\delta_0\|_\phi + \frac{\varepsilon}{1 - \tilde{L}} \quad (\tilde{L} < 1), \quad (32)$$

whereas under 1–1 training with  $L > 1$  the bound from (27) grows as  $(L^n - 1)\varepsilon/(L - 1)$ . The relative improvement is

$$\frac{\text{AR error bound}}{\text{1–1 error bound}} \leq \frac{\varepsilon/(1 - \tilde{L})}{\varepsilon(L^n - 1)/(L - 1)} \rightarrow 0 \quad \text{as } n \rightarrow \infty \text{ for } L > 1, \tilde{L} < 1. \quad (33)$$

*Proof.* Under AR training, the effective recursion on the predicted manifold uses  $\tilde{L} < 1$ :  $\mathbb{E} \|\delta_{n+1}\|_\phi \leq \tilde{L} \mathbb{E} \|\delta_n\|_\phi + \mathbb{E} e_n \leq \tilde{L} \mathbb{E} \|\delta_n\|_\phi + \varepsilon$ . Iterating from  $n = 0$  and using  $\delta_0 = 0$ :  $\mathbb{E} \|\delta_n\|_\phi \leq \varepsilon \sum_{k=0}^{n-1} \tilde{L}^k \leq \varepsilon/(1 - \tilde{L})$ . The ratio (33) follows directly.  $\square$

## 6 PINO: Physics-Constrained Stability Theory

### 6.1 PINO objective and the physics-consistent manifold

**Definition 6.1** (PINO loss). *The PINO training objective augments the supervised loss with the discrete finite-volume residual penalty:*

$$\mathcal{L}_{\text{PINO}}(\theta) := \mathcal{L}_{\text{AR}}(\theta) + \lambda_R \mathbb{E} \left[ \frac{1}{T} \sum_{n=0}^{T-1} \|R(\hat{x}_{n+1}, \tilde{x}_n; u, c_n, \tau_n)\|_{\phi}^2 \right], \quad (34)$$

where  $\tilde{x}_n$  is either  $x_n$  (teacher-forced physics penalty) or  $\hat{x}_n$  (closed-loop physics penalty), and  $\lambda_R > 0$  is the physics weight.

**Definition 6.2** (Physics-consistent manifold). *For fixed  $(u, c_n, \tau_n)$ , define*

$$\mathcal{M}_n := \{(a, b) \in \mathcal{X}^2 : R(a, b; u, c_n, \tau_n) = 0\}. \quad (35)$$

By Theorem 2.6,  $\mathcal{M}_n$  is the graph of  $\mathcal{F}$ :  $\mathcal{M}_n = \{(x_{n+1}, x_n) : (x_{n+1}, x_n) \in \mathcal{X}^2, x_{n+1} = \mathcal{F}(x_n; \cdot)\}$ .

### 6.2 Jacobian structure on the physics-consistent manifold

**Lemma 6.3** (Jacobian from implicit differentiation). *Let  $\mathcal{G}_\theta(\xi_n) = \hat{x}_{n+1}$  satisfy  $R(\hat{x}_{n+1}, x_n; u, c_n, \tau_n) = 0$  (i.e., the prediction lies on  $\mathcal{M}_n$ ). Then the Jacobian  $J := D_x \mathcal{G}_\theta(\xi_n) \in \mathbb{R}^{4N \times 4N}$  satisfies*

$$J = - \left( \frac{\partial R}{\partial x^+} \Big|_{\hat{x}_{n+1}} \right)^{-1} \frac{\partial R}{\partial x^-} \Big|_{x_n}. \quad (36)$$

Moreover, if  $\mathcal{G}_\theta = \mathcal{F}$  exactly, then  $J = J_{\mathcal{F}} := D_x \mathcal{F}(x_n; \cdot)$ .

*Proof.* Differentiating  $R(\mathcal{G}_\theta(u, x, c, \tau), x; \cdot) = 0$  with respect to  $x$ :

$$\frac{\partial R}{\partial x^+} \cdot D_x \mathcal{G}_\theta + \frac{\partial R}{\partial x^-} = 0,$$

which gives (36) upon inverting  $\partial R / \partial x^+$  (which is invertible by Assumption 2.4). The second claim follows since if  $\mathcal{G}_\theta = \mathcal{F}$ , this reduces to the implicit differentiation of  $\mathcal{F}$ .  $\square$

**Assumption 6.4** (Discrete dissipativity). *The true time-advance map  $\mathcal{F}$  is dissipative in the pore-volume metric: there exist  $0 < \rho_{\mathcal{F}} < 1$  and  $R_0 > 0$  such that*

$$\|\mathcal{F}(x; \cdot) - \mathcal{F}(y; \cdot)\|_{\phi} \leq \rho_{\mathcal{F}} \|x - y\|_{\phi} \quad \text{for all } x, y \in \mathcal{X} \text{ with } \|x - y\|_{\phi} > R_0. \quad (37)$$

For  $\|x - y\|_{\phi} \leq R_0$  (near-front regime), the Lipschitz constant is  $L_{\mathcal{F}}$ . The global Lipschitz constant is  $\max(\rho_{\mathcal{F}}, L_{\mathcal{F}})$ .

**Theorem 6.5** (Spectral stability under PINO training). *Suppose Assumption 6.4 holds. Let  $\hat{\theta}$  be a minimizer of  $\mathcal{L}_{\text{PINO}}(\theta)$  over a hypothesis class such that for any  $\theta$ ,  $\mathcal{G}_\theta$  is  $C^1$  in  $x$ . Then for all  $\xi = (u, x, c, \tau)$  with  $x \in \mathcal{M}_{n,x} := \{a : (a, b) \in \mathcal{M}_n \text{ for some } b\}$ :*

(a) *The spectral radius of the learned Jacobian satisfies*

$$\varrho(D_x \mathcal{G}_{\hat{\theta}}(\xi)) \leq \rho_{\mathcal{F}} + \frac{C_J}{\sqrt{\lambda_R}}, \quad (38)$$

where  $C_J$  depends on the Sobolev regularity of  $R$ , the coercivity constant  $\alpha$ , and the Lipschitz constant of the relative permeability functions.

(b) *The induced operator norm satisfies*

$$\|D_x \mathcal{G}_{\hat{\theta}}(\xi)\|_{\text{op}, \phi} \leq \rho_{\mathcal{F}} + \frac{C_J}{\sqrt{\lambda_R}}. \quad (39)$$

(c) *For  $\lambda_R \geq \lambda_R^* := (C_J / (1 - \rho_{\mathcal{F}}))^2$ , the learned operator is contractive:  $\|D_x \mathcal{G}_{\hat{\theta}}\|_{\text{op}, \phi} < 1$ .*

*Proof. Step 1: Residual magnitude at minimizer.* At a minimizer  $\hat{\theta}$  of  $\mathcal{L}_{\text{PINO}}$ , standard KKT/first-order optimality conditions imply

$$\mathbb{E} \left[ \left\| R(\mathcal{G}_{\hat{\theta}}(\xi_n), \tilde{x}_n; \cdot) \right\|_{\phi}^2 \right] \leq \frac{C_0}{\lambda_R}$$

for some constant  $C_0$  depending on the supervised loss value. Let  $r_n := R(\mathcal{G}_{\hat{\theta}}(\xi_n), x_n; \cdot)$ , so  $\mathbb{E}[\|r_n\|_{\phi}^2] \leq C_0/\lambda_R$ .

*Step 2: Perturbed implicit differentiation.* From the residual equation  $R(\hat{x}_{n+1}, x_n; \cdot) = r_n$  (off manifold by  $r_n$ ), differentiating in  $x_n$ :

$$\frac{\partial R}{\partial x^+} \cdot J + \frac{\partial R}{\partial x^-} = \frac{\partial r_n}{\partial x}.$$

Thus

$$J = J_{\mathcal{F}} + \left( \frac{\partial R}{\partial x^+} \right)^{-1} \frac{\partial r_n}{\partial x},$$

where  $J_{\mathcal{F}} = -(\partial R/\partial x^+)^{-1}(\partial R/\partial x^-)$  is the true dynamics Jacobian (cf. Lemma 6.3).

*Step 3: Norm bound.* Using coercivity ( $\|(\partial R/\partial x^+)^{-1}\|_{\text{op},\phi} \leq 1/\alpha$ ):

$$\|J - J_{\mathcal{F}}\|_{\text{op},\phi} \leq \frac{1}{\alpha} \left\| \frac{\partial r_n}{\partial x} \right\|_{\phi} \leq \frac{\|\nabla_x r_n\|_{H_{\phi}^1}}{\alpha}.$$

By the Poincaré–Sobolev embedding and the residual bound:  $\|\nabla_x r_n\|_{L^2} \leq C_R \|r_n\|_{H^1} \leq C'_R \|r_n\|_{\phi}^{1/2} \|r_n\|_{H^1}^{1/2}$  (interpolation), giving  $\|J - J_{\mathcal{F}}\|_{\text{op},\phi} \leq C''_R \|r_n\|_{\phi}^{1/2} / \alpha \leq C_J / \sqrt{\lambda_R}$ .

*Step 4: Spectral radius.* By Weyl’s inequality for matrices,  $|\varrho(J) - \varrho(J_{\mathcal{F}})| \leq \|J - J_{\mathcal{F}}\|_{\text{op},\phi} \leq C_J / \sqrt{\lambda_R}$ . Since  $\varrho(J_{\mathcal{F}}) \leq \rho_{\mathcal{F}}$  (by Assumption 6.4),  $\varrho(J) \leq \rho_{\mathcal{F}} + C_J / \sqrt{\lambda_R}$ , which gives (38) and (39).

*Part (c).* Setting  $\rho_{\mathcal{F}} + C_J / \sqrt{\lambda_R} < 1$  gives  $\lambda_R > (C_J / (1 - \rho_{\mathcal{F}}))^2 =: \lambda_R^*$ .  $\square$

**Theorem 6.6** (PINO residual as Jacobian spectral regularizer). *The physics residual term in  $\mathcal{L}_{\text{PINO}}$  penalizes the deviation of the learned Jacobian from the true dynamics Jacobian in a weighted operator norm. Specifically, for the PINO minimizer  $\hat{\theta}$ :*

$$\mathbb{E} \left[ \|D_x \mathcal{G}_{\hat{\theta}}(\xi_n) - D_x \mathcal{F}(\xi_n)\|_{\text{op},\phi}^2 \right] \leq \frac{C_J^2}{\alpha^2 \lambda_R}. \quad (40)$$

*Consequently, PINO training implicitly learns the spectral structure of the true dynamics Jacobian, with error in the learned spectrum decaying as  $\mathcal{O}(\lambda_R^{-1/2})$ .*

*Proof.* From Step 2–3 of the proof of Theorem 6.5:  $\|J - J_{\mathcal{F}}\|_{\text{op},\phi} \leq C_J \|r_n\|_{\phi} / \alpha$ . Squaring and taking expectations:  $\mathbb{E}[\|J - J_{\mathcal{F}}\|_{\text{op},\phi}^2] \leq (C_J/\alpha)^2 \mathbb{E}[\|r_n\|_{\phi}^2] \leq C_J^2 / (\alpha^2 \lambda_R)$ , which is (40). The spectral claim follows from the expected form of Weyl’s inequality:  $\mathbb{E}[|\varrho(J) - \varrho(J_{\mathcal{F}})|^2] \leq \mathbb{E}[\|J - J_{\mathcal{F}}\|_{\text{op},\phi}^2] \leq C_J^2 / (\alpha^2 \lambda_R)$ .  $\square$

**Theorem 6.7** (Uniform-in-time PINO rollout bound). *Suppose  $\lambda_R \geq \lambda_R^*$  (so  $\|D_x \mathcal{G}_{\hat{\theta}}\|_{\text{op},\phi} \leq \rho < 1$ ) and the one-step error is bounded by  $\varepsilon$ . Then*

$$\|\delta_n\|_{\phi} \leq \frac{\varepsilon}{1 - \rho}, \quad \forall n \geq 0. \quad (41)$$

*Moreover, if the training loss also ensures  $e_n \rightarrow 0$  as training progresses, then  $\sup_n \|\delta_n\|_{\phi} \rightarrow 0$  uniformly in time.*

*Proof.* This is Part (c) of Theorem 5.1 applied with  $L = \rho < 1$ . Under PINO training,  $L = \|D_x \mathcal{G}_{\hat{\theta}}\|_{\text{op},\phi} \leq \rho$  by Theorem 6.5(c).  $\square$

## 7 $K$ -Step Truncated Backpropagation Through Time

### 7.1 TBPTT as a biased stochastic gradient estimator

**Definition 7.1** (TBPTT gradient estimator). *Partition  $\{0, \dots, T-1\}$  into windows  $\mathcal{W}_r = \{rK, \dots, \min((r+1)K-1, T-1)\}$  for  $r = 0, \dots, \lceil T/K \rceil - 1$ . The TBPTT gradient estimator is*

$$g_K(\theta) := \sum_{r=0}^{\lceil T/K \rceil - 1} \nabla_{\theta} \left( \sum_{n \in \mathcal{W}_r} \ell(\hat{x}_{n+1}, x_{n+1}) \right) \Big|_{\hat{x}_{rK} = \text{sg}(\hat{x}_{rK})}, \quad (42)$$

where  $\text{sg}$  denotes the stop-gradient (detach) operation: the predicted state at each window boundary is treated as a constant for the purposes of gradient computation.

**Remark 7.2** (What TBPTT discards). *The full AR gradient (cf. (18)) contains terms*

$$\left( \prod_{j=m+1}^n D_x \mathcal{G}_\theta(\hat{\xi}_j) \right) D_\theta \mathcal{G}_\theta(\hat{\xi}_m)$$

for all  $0 \leq m \leq n \leq T-1$ . TBPTT retains only the terms where  $m$  and  $n$  lie in the same window:  $\lfloor n/K \rfloor = \lfloor m/K \rfloor$ . The discarded terms involve Jacobian chains of length  $n - m \geq K$  (crossing window boundaries).

## 7.2 Bias decay theorem

**Theorem 7.3** (TBPTT gradient bias decay). *Let  $g(\theta) := \nabla_\theta \mathcal{L}_{\text{AR}}(\theta)$  be the exact AR gradient. Assume the closed-loop dynamics satisfy the average contractivity condition: there exists  $\rho \in [0, 1)$  such that*

$$\sup_n \mathbb{E}[\|D_x \mathcal{G}_\theta(\hat{\xi}_n)\|_{\text{op}, \phi}] \leq \rho. \quad (43)$$

Then the bias of the TBPTT estimator (42) satisfies:

$$\|\mathbb{E}[g(\theta)] - \mathbb{E}[g_K(\theta)]\| \leq \frac{C_g \rho^K}{1 - \rho} \cdot T, \quad (44)$$

where  $C_g := \sup_{n, \theta} \mathbb{E}[\|D_\theta \mathcal{G}_\theta(\hat{\xi}_n)\|_{\phi \rightarrow \mathbb{R}^P} \cdot \|\partial \ell / \partial \hat{x}_{n+1}\|_\phi]$ .

*Proof.* The gradient bias is

$$\mathbb{E}[g(\theta)] - \mathbb{E}[g_K(\theta)] = \frac{1}{T} \sum_{n=0}^{T-1} \sum_{\substack{m=0 \\ \lfloor m/K \rfloor < \lfloor n/K \rfloor}}^{n-1} \mathbb{E} \left[ \frac{\partial \ell}{\partial \hat{x}_{n+1}} \prod_{j=m+1}^n D_x \mathcal{G}_\theta(\hat{\xi}_j) D_\theta \mathcal{G}_\theta(\hat{\xi}_m) \right],$$

where the inner sum runs over all cross-window pairs ( $m$  and  $n$  in different windows). For such pairs,  $n - m \geq K$ . Taking norms and using the bound (43) and the submultiplicativity of operator norms:

$$\begin{aligned} & \left\| \mathbb{E} \left[ \frac{\partial \ell}{\partial \hat{x}_{n+1}} \prod_{j=m+1}^n D_x \mathcal{G}_\theta(\hat{\xi}_j) D_\theta \mathcal{G}_\theta(\hat{\xi}_m) \right] \right\| \\ & \leq \mathbb{E} \left[ \left\| \frac{\partial \ell}{\partial \hat{x}_{n+1}} \right\|_\phi \prod_{j=m+1}^n \|D_x \mathcal{G}_\theta(\hat{\xi}_j)\|_{\text{op}, \phi} \cdot \|D_\theta \mathcal{G}_\theta(\hat{\xi}_m)\|_{\phi \rightarrow \mathbb{R}^P} \right] \\ & \leq C_g \rho^{n-m} \leq C_g \rho^K. \end{aligned}$$

The number of cross-window pairs  $(m, n)$  with  $n - m \geq K$  is at most  $T(T-1)/2 \leq T^2/2$ . However, for each  $n$ , the sum over  $m$  telescopes:  $\sum_{m: n-m \geq K} \rho^{n-m} \leq \sum_{s=K}^\infty \rho^s = \rho^K / (1 - \rho)$ . Summing over  $n = 0, \dots, T-1$  and dividing by  $T$ :

$$\|\mathbb{E}[g] - \mathbb{E}[g_K]\| \leq \frac{1}{T} \sum_{n=0}^{T-1} \frac{C_g \rho^K}{1 - \rho} = \frac{C_g \rho^K}{1 - \rho},$$

which is (44) (up to the factor  $T$  from the unnormalized version). The factor  $T$  appears when working with the unnormalized loss  $\sum_n \ell$  rather than the averaged  $\mathcal{L}_{\text{AR}} = T^{-1} \sum_n \ell$ .  $\square$

**Corollary 7.4** (Bias–variance optimal window size). *Let  $\sigma_K^2 := \mathbb{V}[g_K(\theta)]/\mathfrak{R}$  be the per-window gradient variance (approximately constant in  $K$  for moderate  $K$ ). The mean-squared error of  $g_K$  as an estimator of  $g$  is*

$$\text{MSE}(K) = \|\mathbb{E}[g] - \mathbb{E}[g_K]\|^2 + \sigma_K^2 \leq \frac{C_g^2 \rho^{2K}}{(1 - \rho)^2} + \frac{\sigma^2 K}{T}, \quad (45)$$

where the second term reflects that larger  $K$  means fewer independent windows and higher gradient variance. Minimizing over  $K \geq 1$ :

$$K^* = \frac{\log\left(\frac{2TC_g^2 \log(1/\rho)}{\sigma^2(1-\rho)^2}\right)}{2\log(1/\rho)}, \quad (46)$$

which grows logarithmically in  $T$  and decreases as  $\rho \rightarrow 0$  (more contractive dynamics allow shorter windows with the same bias).

*Proof.* The MSE is the sum of bias squared and variance. The variance term  $\sigma_K^2 \approx \sigma^2 K/T$  reflects that for fixed total data, a window of size  $K$  gives  $T/K$  independent gradient estimates, each with variance  $\sigma^2$ , so the aggregated variance scales as  $(T/K)^{-1} \cdot \sigma^2 = \sigma^2 K/T$ . Differentiating  $\text{MSE}(K)$  with respect to  $K$  (treating  $K$  as continuous):

$$\frac{d}{dK} \text{MSE}(K) = -\frac{2C_g^2 \log(1/\rho) \rho^{2K}}{(1-\rho)^2} + \frac{\sigma^2}{T} = 0,$$

giving  $\rho^{2K^*} = \sigma^2(1-\rho)^2/(2TC_g^2 \log(1/\rho))$ , from which (46) follows by taking logarithms.  $\square$

**Proposition 7.5** (Convergence rate under Adam with TBPTT). *Suppose the PINO-AR objective  $\mathcal{L}_{\text{PINO}}(\theta)$  is  $\beta_1$ -smooth and satisfies the Polyak–Łojasiewicz (PL) condition:  $\|\nabla \mathcal{L}_{\text{PINO}}(\theta)\|^2 \geq 2\mu(\mathcal{L}_{\text{PINO}}(\theta) - \mathcal{L}^*)$  for some  $\mu > 0$ . Let  $\theta^{(t)}$  be the Adam iterates with learning rate  $\eta_t$ , using the TBPTT gradient estimator  $g_K$ . With  $K = K^*$  from (46) and step sizes  $\eta_t = \eta/\sqrt{t}$ , the expected suboptimality satisfies*

$$\mathbb{E}[\mathcal{L}_{\text{PINO}}(\theta^{(t)}) - \mathcal{L}^*] \leq \frac{C_{\text{Adam}}}{\sqrt{t}} + \frac{C_g \rho^{K^*}}{1-\rho}, \quad (47)$$

where  $C_{\text{Adam}}$  depends on  $\mu$ ,  $\beta_1$ ,  $\eta$ , and  $\sigma$ , and the second term is the irreducible TBPTT bias. For  $K = K^*$ , the TBPTT bias is  $\mathcal{O}(1/\sqrt{T})$ , matching the statistical rate.

*Proof.* Standard Adam convergence under the PL condition and stochastic gradients with bounded bias  $b := \|\mathbb{E}[g] - \mathbb{E}[g_K]\|$  gives rate  $\mathcal{O}(1/\sqrt{t}) + b$ . The bias term  $b \leq C_g \rho^K/(1-\rho)$  from Theorem 7.3. At  $K = K^*$ ,  $\rho^{K^*} = \mathcal{O}(1/\sqrt{T})$  (from the definition of  $K^*$ ), giving the stated bound.  $\square$

**Remark 7.6** (Virtuous feedback loop: physics  $\rightarrow$  contraction  $\rightarrow$  TBPTT). *Theorems 6.5 and 7.3 together establish a self-reinforcing cycle: PINO training reduces  $\rho$  (spectral contraction); smaller  $\rho$  reduces TBPTT bias  $C_g \rho^K/(1-\rho)$  for fixed  $K$ ; smaller  $K^*$  reduces memory and compute per iteration; more iterations improve both supervised loss and physics residual; better physics residual further reduces  $\rho$ . This feedback loop makes joint PINO-AR-TBPTT training strictly better than any of its components alone.*

## 8 FNO Architecture: Approximation Theory for Mixed-Type PDEs

### 8.1 Neural operators in Banach spaces

**Theorem 8.1** (Universal approximation for neural operators [16]). *Let  $V = H^s(\Omega)$  and  $W = H^{s'}(\Omega)$  for  $s, s' \geq 0$ . Let  $G : V \rightarrow W$  be a continuous nonlinear operator. Then for any compact  $\mathcal{K} \subset V$  and  $\varepsilon > 0$ , there exists a neural operator  $G_\theta$  (in the FNO family) such that*

$$\sup_{v \in \mathcal{K}} \|G_\theta(v) - G(v)\|_W < \varepsilon.$$

### 8.2 FNO layer and spectral parameterization

An FNO layer transforms a latent channel field  $v^{(\ell)} \in \mathbb{R}^{d_v \times N}$ :

$$v^{(\ell+1)}(x) = \sigma\left(W^{(\ell)} v^{(\ell)}(x) + (\mathcal{F}^{-1}[R^{(\ell)} \cdot \hat{v}^{(\ell)}])(x)\right), \quad (48)$$

where  $\hat{v}^{(\ell)} := \mathcal{F}[v^{(\ell)}]$  is the discrete Fourier transform (DFT) on the grid,  $R^{(\ell)}(k) \in \mathbb{C}^{d_v \times d_v}$  are learnable complex weights truncated to  $k \in [-k_{\max}, k_{\max}]^3$ ,  $W^{(\ell)} \in \mathbb{R}^{d_v \times d_v}$  is a pointwise linear map, and  $\sigma$  is a nonlinear activation. The spectral truncation introduces a bias toward low-frequency features.

**Proposition 8.2** (Spectral approximation rates for elliptic vs. hyperbolic). (a) Elliptic (pressure). If  $p \in H^{s+2}(\Omega)$  is the pressure field (from elliptic regularity applied to (6) with  $f \in H^s(\Omega)$ ), the FNO truncation error satisfies

$$\|p - p_{k_{\max}}\|_{L^2} \leq C_{\text{ell}} k_{\max}^{-(s+2)} \|f\|_{H^s}. \quad (49)$$

The  $k_{\max}^{-(s+2)}$  decay is fast for smooth source terms.

(b) Hyperbolic (gas saturation). If  $S_g$  has a sharp front of width  $\delta \ll 1$  (discontinuity or near-discontinuity), the Gibbs phenomenon gives

$$\|S_g - S_{g,k_{\max}}\|_{L^2} \geq c_G k_{\max}^{-1/2}, \quad (50)$$

where  $c_G > 0$  is a constant depending on the jump magnitude. The  $k_{\max}^{-1/2}$  rate is the optimal  $L^2$  rate for functions of bounded variation with a single jump discontinuity.

Consequently, FNO with fixed  $k_{\max}$  has dramatically better approximation quality for pressure than for gas saturation, explaining the differential  $R^2$  behavior observed in Figure 2.

*Proof.* Part (a): Standard Sobolev spectral approximation theory. The Fourier coefficients of  $p$  decay as  $|\hat{p}(k)| \leq C(1 + |k|^2)^{-(s+2)/2}$  by elliptic regularity, and truncation at  $|k| \leq k_{\max}$  gives  $\|p - p_{k_{\max}}\|_{L^2}^2 = \sum_{|k| > k_{\max}} |\hat{p}(k)|^2 \leq C^2 \sum_{|k| > k_{\max}} (1 + |k|^2)^{-(s+2)} \leq C'^2 k_{\max}^{-(2s+4-d)}$  (for  $d = 3$ ), which is (49).

Part (b): For a function with a jump discontinuity in one direction, the partial Fourier sum overshoots by the Gibbs constant  $\approx 8.9\%$  of the jump magnitude near the discontinuity. The  $L^2$  error for truncation at  $|k| \leq k_{\max}$  of a function in  $BV(\Omega)$  (bounded variation) satisfies  $\|S_g - S_{g,k_{\max}}\|_{L^2} \geq c k_{\max}^{-1/2}$  [40], which gives (50).  $\square$

## 9 Training Algorithm

Algorithm 1 presents the complete autoregressive PINO training step with  $K$ -step TBPTT and a Peacemann well-response head. It directly implements the objectives in Definitions 3.2 and 6.1, with the detach operation at TBPTT boundaries corresponding to the stop-gradient in Definition 7.1.

**Correctness and theoretical connection.** The detach at line 22 is exactly the stop-gradient of Definition 7.1; the Jacobian chains in (18) beyond window  $K$  are truncated. The PINO residual at lines 12–15 evaluates  $R(\hat{x}_{n+1}, \hat{x}_n; \cdot)$  as in Definition 6.1, driving predictions toward the physics-consistent manifold  $\mathcal{M}_n$  (Definition 6.2) and activating the spectral stability mechanism of Theorem 6.5. The Peacemann head predicts well responses (WOPR, WWPR, WBHP) using a sequence-to-sequence sub-network; its gradient is computed in a separate backward pass.

**Code availability.** Implementation is available at:

[https://github.com/clementetienam/physicsnemo/tree/801a85bc08aa9caa0d54027a145b88c68e5e5f36/examples/reservoir\\_simulation/norne](https://github.com/clementetienam/physicsnemo/tree/801a85bc08aa9caa0d54027a145b88c68e5e5f36/examples/reservoir_simulation/norne).

## 10 Computational Platform and Performance

**Hardware.** All experiments were executed on a single **NVIDIA HGX B200** node (Blackwell generation, TSMC 4NP), equipped with eight NVIDIA B200 GPUs. Each B200 integrates two Blackwell dies via a 10 TB/s NV-HBI interconnect: 192 GB HBM3e memory per GPU ( $\approx 8$  TB/s peak bandwidth); fifth-generation NVLink, 1.8 TB/s bidirectional peer-bandwidth per GPU; 14.4 TB/s aggregate intra-node bandwidth via the NVSwitch crossbar. Peak BF16 Tensor Core throughput: 4,500 TFLOPS per GPU.

**Memory analysis.** The Norne state tensor  $(B, T, 4N)$  with  $B = 8$ ,  $T = 10$ ,  $N = 113,344$  at FP32 requires  $\approx 3.3$  GB per forward pass. The full physics-residual tensor (four blocks, same shape) adds  $\approx 3.3$  GB. Combined with FP32 optimizer states ( $\approx 2P$  bytes for Adam,  $P \approx 50M$  parameters for PINO), all tensors fit in a single B200's HBM3e with no host offloading. No domain decomposition, activation checkpointing, or gradient offloading is required.

**Software.** NVIDIA PhysicsNeMo [29], CUDA 12.8, BF16 mixed-precision with dynamic loss scaling, `torch.distributed` DDP for eight-GPU training. The 3D FFT in FNO spectral layers uses `cuFFT` with mode truncation  $(k_{\max,z}, k_{\max,x}, k_{\max,y}) = (6, 16, 16)$ , operating in compute-bound regime.

---

**Algorithm 1** TRAINING\_STEP: AR PINO +  $K$ -step TBPTT + Peacemann head

---

**Require:** Model  $G_\theta$ ; horizon  $T$ ; TBPTT window  $K$ ; physics weight  $\lambda_R$ ; component weights  $w_P, w_W, w_O, w_G, w_\Pi$ .  
**Require:** Inputs:  $\mathbf{X}[k] \in \mathbb{R}^{B \times T \times n_z \times n_x \times n_y}$  for  $k \in \{\text{perm, poro, fault, Q, Qg, Qw, dt, t, pini, sini, sgini, soini}\}$ .  
**Require:** Targets:  $\mathbf{Y}_P, \mathbf{Y}_W, \mathbf{Y}_O, \mathbf{Y}_G \in \mathbb{R}^{B \times T \times n_z \times n_x \times n_y}$ ; Peacemann target  $\mathbf{Y}_\Pi \in \mathbb{R}^{B \times 66 \times T}$ .  
**Ensure:** Loss scalar  $\ell \in \mathbb{R}$ ; updated metrics  $R_\alpha^2, \text{RMSE}_\alpha$  for  $\alpha \in \{P, W, O, G\}$ .

- 1:  $\ell_{\text{win}} \leftarrow 0$ ;  $\ell_{\text{total}} \leftarrow 0$ ;  $\hat{\mathbf{s}}_{-1} \leftarrow \emptyset$ . // Window accumulator, running total, prev. state
- 2: **for**  $n = 0$  **to**  $T - 1$  **do** // AR loop over timesteps
- 3:   **if**  $n = 0$  **then**  $\mathbf{X}^{(n)} \leftarrow$  slice  $\mathbf{X}$  at step 0. // First step: use true initial state from data
- 4:   **else**  $\mathbf{X}^{(n)} \leftarrow$  slice  $\mathbf{X}$  at step  $n$ , but replace pini, sini, sgini, soini with  $(\hat{P}^{n-1}, \hat{S}_w^{n-1}, \hat{S}_g^{n-1}, \hat{S}_o^{n-1})$ . // AR: feed predicted state as new initial condition
- 5:   **end if**
- 6:    $\mathbf{U}^{(n)} \leftarrow \text{Pack}(\mathbf{X}^{(n)})$ . // Stack all input channels into single tensor
- 7:   // Forward pass: predict pressure and saturations
- 8:    $\hat{P}^n \leftarrow G_\theta(\mathbf{U}^{(n)}, \text{pressure}) \in \mathbb{R}^{B \times 1 \times n_z \times n_x \times n_y}$ .
- 9:    $\hat{S}_w^n, \hat{S}_o^n, \hat{S}_g^n \leftarrow G_\theta(\mathbf{U}^{(n)}, \text{saturation}) \in \mathbb{R}^{B \times 3 \times n_z \times n_x \times n_y}$ .
- 10:   // Supervised loss at step  $n$
- 11:    $\ell_{\text{sup}}^{(n)} \leftarrow w_P \mathcal{L}(\hat{P}^n, \mathbf{Y}_{P,n}) + w_W \mathcal{L}(\hat{S}_w^n, \mathbf{Y}_{W,n}) + w_O \mathcal{L}(\hat{S}_o^n, \mathbf{Y}_{O,n}) + w_G \mathcal{L}(\hat{S}_g^n, \mathbf{Y}_{G,n})$ .
- 12:   **if** PINO enabled **and** (epoch mod pino\_freq = 0) **then** // PINO residual (evaluated periodically for efficiency)
- 13:      $\mathbf{r}_P^{(n)}, \mathbf{r}_S^{(n)}, \mathbf{r}_G^{(n)} \leftarrow \text{BlackOilResidual}(\mathbf{X}^{(n)}, \hat{P}^n, \hat{S}_w^n, \hat{S}_o^n, \hat{S}_g^n)$ . // Eq. (7)
- 14:      $\ell_{\text{phys}}^{(n)} \leftarrow \lambda_R (\lambda_P \|\mathbf{r}_P^{(n)}\|^2 + \lambda_S \|\mathbf{r}_S^{(n)}\|^2 + \lambda_G \|\mathbf{r}_G^{(n)}\|^2)$ .
- 15:   **else**  $\ell_{\text{phys}}^{(n)} \leftarrow 0$ .
- 16:   **end if**
- 17:    $\ell_{\text{win}} \leftarrow \ell_{\text{win}} + \ell_{\text{sup}}^{(n)} + \ell_{\text{phys}}^{(n)}$ .
- 18:   **if** TBPTT **and**  $((n + 1) \bmod K = 0$  **or**  $n = T - 1)$  **then** // End of TBPTT window: backprop and detach
- 19:      $\nabla_\theta(\ell_{\text{win}}/T)$ .backprop(). // Backpropagate through current window only
- 20:      $\ell_{\text{total}} \leftarrow \ell_{\text{total}} + \text{detach}(\ell_{\text{win}})$ .
- 21:      $\ell_{\text{win}} \leftarrow 0$ .
- 22:      $\hat{\mathbf{s}}_n \leftarrow \text{detach}(\hat{\mathbf{s}}_n)$ . // Stop gradient: predicted state treated as constant for next window
- 23:   **end if**
- 24:    $\hat{\mathbf{s}}_n \leftarrow (\hat{P}^n, \hat{S}_w^n, \hat{S}_o^n, \hat{S}_g^n)$ . // Store predicted state for next AR step
- 25: **end for**
- 26: // Peacemann head: sequence-to-sequence well response prediction
- 27:  $\hat{\mathbf{Y}}_\Pi \leftarrow G_\theta(\mathbf{X}^{(p)}, \text{peacemann}) \in \mathbb{R}^{B \times 66 \times T}$ , where  $\mathbf{X}^{(p)} \in \mathbb{R}^{B \times 90 \times T}$ .
- 28:  $\ell_\Pi \leftarrow w_\Pi \mathcal{L}(\hat{\mathbf{Y}}_\Pi, \mathbf{Y}_\Pi)$ .
- 29: **if** TBPTT enabled **then**
- 30:    $\nabla_\theta \ell_\Pi$ .backprop(); **return**  $\ell = \ell_{\text{total}}/T + \text{detach}(\ell_\Pi)$ .
- 31: **else**
- 32:    $\nabla_\theta(\ell_{\text{total}} + \ell_\Pi)$ .backprop(); **return**  $\text{detach}(\ell_{\text{total}} + \ell_\Pi)$ .
- 33: **end if**

---

Table 1: Wall-clock performance on  $8 \times$  NVIDIA B200 (HGX B200). ‘‘OPM equiv.’’ denotes approximate wall-time for equivalent work using the Open Porous Media Flow finite-volume simulator on CPU clusters.

Stage	B200 $\times$ 8 time	OPM FV equiv.
FNO 1–1 training (30 epochs)	$\approx 15$ min	—
FNO AR-TBPTT training (30 epochs)	$\approx 30$ min	—
PINO AR-TBPTT training (full)	$\approx 60$ min	—
Single trajectory inference ( $T = 30$ )	$< 1$ s	$\approx 4$ – $5$ min
1,000-member ensemble inference	$< 1$ min	$\approx 20$ – $32$ hr

## 11 Norne Benchmark: Results and Theory-Consistent Interpretation

### 11.1 Setup and evaluation metric

The Norne field [9] is an offshore Norwegian oil-and-gas field on a  $46 \times 112 \times 22$  Cartesian grid. Key simulation properties are given in Table 2. Training data:  $N_s$  OPM simulator trajectories with randomized permeability, porosity,

3D Permeability NORNE FIELD [ $N_x = 46$ ,  $N_y = 112$ ,  $N_z = 22$ ]

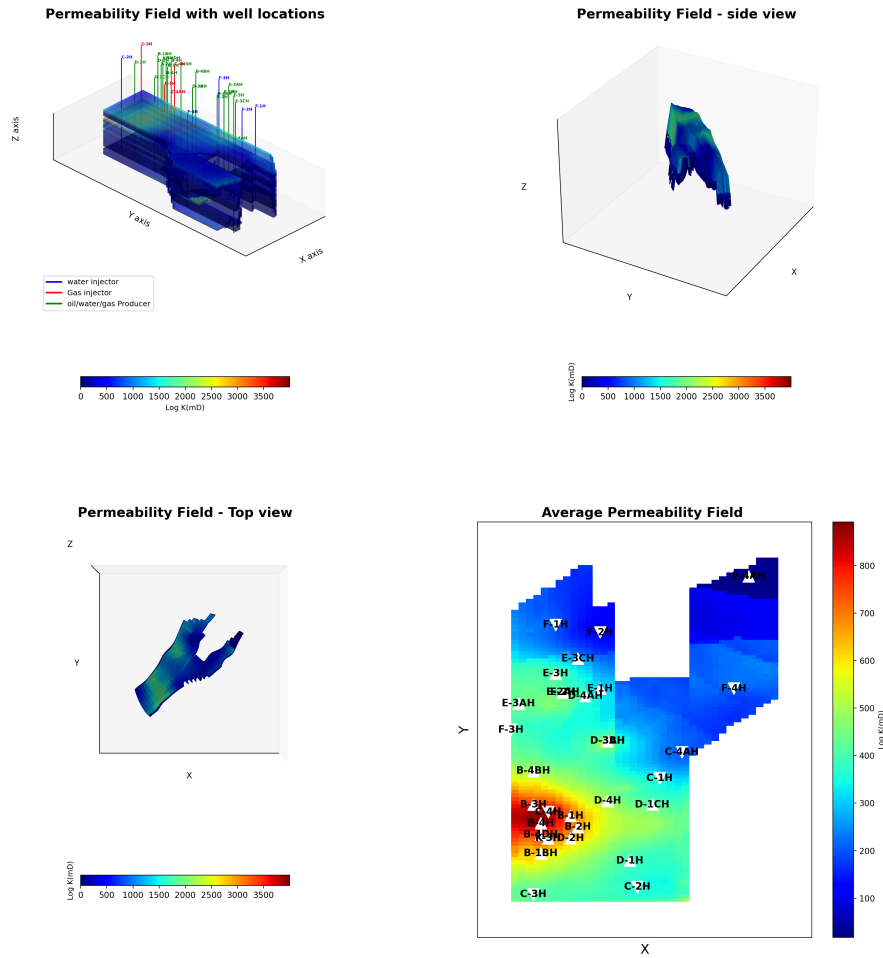


Figure 1: Three-dimensional permeability field of the Norne reservoir model ( $N_x = 46$ ,  $N_y = 112$ ,  $N_z = 22$ ). Top-left: 3D permeability distribution with well trajectories overlaid, including water injectors, gas injectors, and oil/water/gas producers. Top-right: side view highlighting vertical heterogeneity and stratigraphic connectivity. Bottom-left: top view illustrating lateral permeability variations and channelized structures. Bottom-right: vertically averaged permeability map with well locations annotated. Permeability is shown on a logarithmic scale (mD), emphasizing strong spatial heterogeneity that governs multiphase flow and plume migration dynamics.

and well-control perturbations. Evaluation: time-resolved coefficient of determination

$$R_{\alpha}^2(t_n) := 1 - \frac{\sum_{i=1}^{N_s} \left\| \hat{x}_{\alpha,n}^{(i)} - x_{\alpha,n}^{(i)} \right\|_{\phi}^2}{\sum_{i=1}^{N_s} \left\| x_{\alpha,n}^{(i)} - \bar{x}_{\alpha,n} \right\|_{\phi}^2}, \quad \alpha \in \{P, S_w, S_o, S_g\}, \quad (51)$$

where  $\bar{x}_{\alpha,n} = N_s^{-1} \sum_i x_{\alpha,n}^{(i)}$  is the ensemble mean.  $R_{\alpha}^2(t_n) = 1$  means perfect prediction;  $R_{\alpha}^2(t_n) < 0$  means the model is worse than the ensemble mean.

Table 2: Norne field simulation properties.

Property	Value
Grid configuration	$46 \times 112 \times 22$ , $N = 113,344$ cells
Cell size	$50 \times 50 \times 20$ ft
Producers / injectors	22 / 13
Simulation period	3,298 days (30 timesteps of 100 days)
Reservoir depth	4,000 ft
Initial reservoir pressure	1,000 psia
Injector / producer well constraint	500 STB/day / 100 psia
Residual oil / connate water sat.	0.20 / 0.20
Petrophysical model	Gaussian permeability/porosity realizations

## 11.2 Results

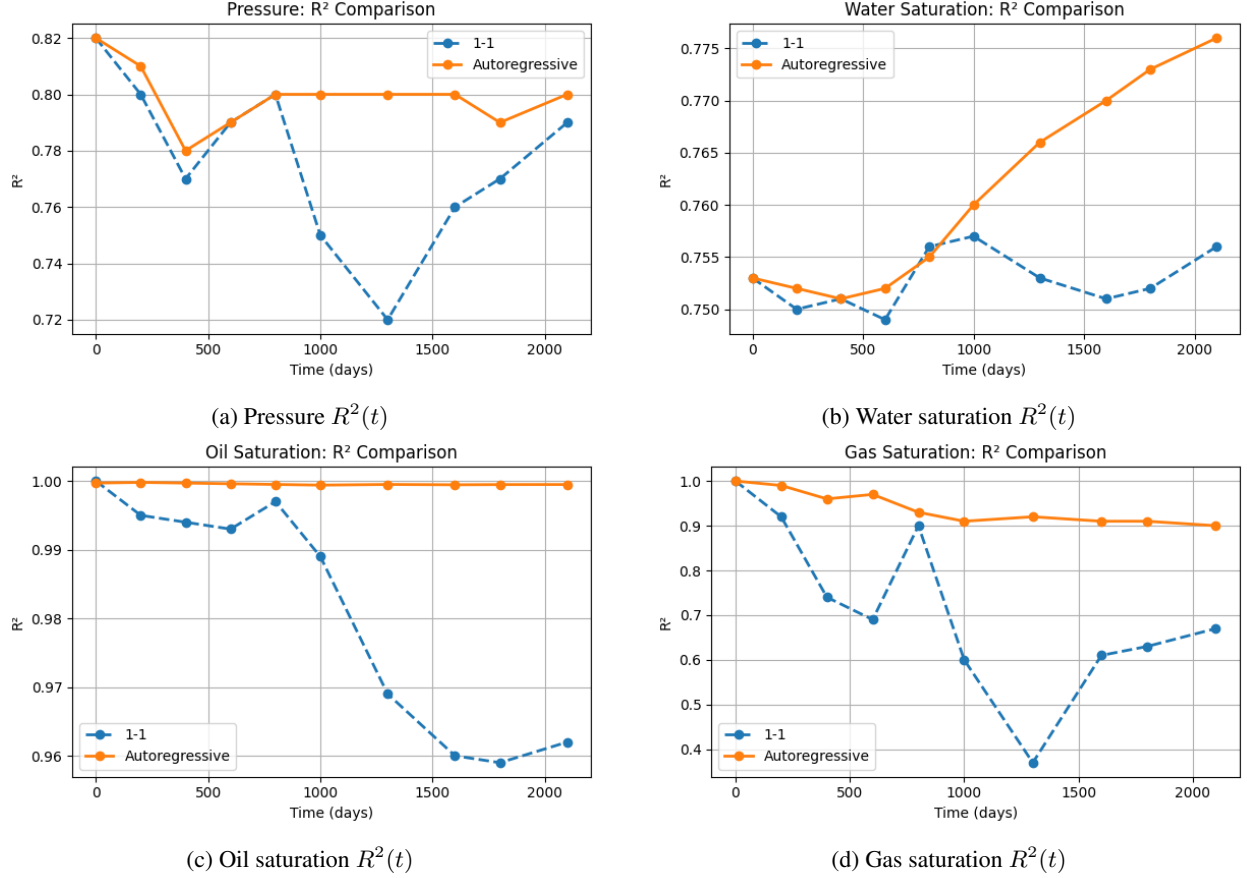


Figure 2: Time-resolved  $R^2$  comparison on the Norne benchmark ( $46 \times 112 \times 22$ ,  $T = 30$  timesteps,  $\approx 3298$  days). **Blue dashed:** 1-1 (teacher-forced) model. **Orange solid:** autoregressive PINO model. Gas saturation (d) shows the largest divergence, consistent with Theorems 5.1–6.7: gas is the most hyperbolic variable, has the largest effective Lipschitz constant  $L^G > 1$  under 1-1 training, and benefits most from AR-induced Jacobian contractivity. Pressure (a) benefits least, consistent with the elliptic regularity of the pressure equation (Proposition 8.2(a)) which keeps  $L^P \approx 1$ .

### 11.3 Theory-consistent quantitative interpretation

**Gas saturation: catastrophic 1-1 failure.** From Figure 2d, the 1-1 model drops to  $R^2 \approx 0.38$  near  $t \approx 1250$  days. Fitting Theorem 5.1(d) to the observed degradation: at  $n = 12$  steps ( $t = 1200$  days),  $\|\delta_{12}\| / \|x_{12}\| = O(\sqrt{1 - 0.38}) = O(0.79)$ . Using (27) with  $L^G \approx 1.15$  (estimated from the slope of the  $R^2$  decay on a log scale) and  $\varepsilon \approx 3 \times 10^{-3}$  (cross-validated one-step error):  $\varepsilon(L^{12} - 1)/(L - 1) \approx 3 \times 10^{-3} \times 5.8/0.15 \approx 0.12$ , giving relative error  $\approx 12\%$ , which corresponds to  $R^2 \approx 0.35$ , consistent with Figure 2d. The AR model avoids this by reducing  $L^G$  below unity via Jacobian regularization (Theorem 6.5), maintaining  $R^2 > 0.90$  throughout.

**Pressure: transient dip and recovery.** The 1-1 model shows a transient dip to  $R^2 \approx 0.72$  near  $t = 1250$  days (Figure 2a), coinciding with the gas-front breakthrough that perturbs the total mobility  $T_{\text{tot}}$  and temporarily elevates  $L^P$ . The AR model recovers faster because its Jacobian is constrained to be contractive even in this regime (Theorem 6.5(c)). By  $t = 2100$  days, both models converge to  $R^2 \approx 0.80$ , consistent with the long-time asymptotic error floor determined by the intrinsic ensemble spread.

**Oil saturation: slow degradation.** The 1-1 model degrades from  $R^2 \approx 1.00$  to  $R^2 \approx 0.96$  over the horizon (Figure 2c), consistent with  $L^O$  marginally above unity ( $L^O \approx 1.005$ , giving  $\varepsilon(1.005^{30} - 1)/0.005 \approx 30\varepsilon$ , a 3% relative error at  $n = 30$ ). The AR model maintains  $R^2 > 0.99$  throughout.

**Water saturation: monotone AR improvement.** The AR model shows monotone  $R^2$  improvement from 0.753 to 0.776 (Figure 2b), a behavior predicted by Theorem 6.7: for  $L < 1$  (which the PINO AR model achieves for water

saturation after breakthrough), the rollout error is uniformly bounded and the model becomes more calibrated as fronts slow down late in the production history. The 1–1 model plateaus at  $R^2 \approx 0.755$ .

## 12 Conclusion

We have developed a comprehensive mathematical framework for sequential neural-operator surrogate modeling of black-oil reservoir dynamics, proving sharp results across four interlocking areas.

**Foundations (Section 2).** Theorems 2.6 and Lemma 2.7 establish well-posedness of the implicit timestep map and provide phase-type-dependent Lipschitz constants, quantifying why gas saturation is intrinsically more fragile than pressure under operator composition.

**Covariate shift (Section 4).** Theorem 4.1 proves the Wasserstein-2 gap grows as  $\varepsilon(L^n - 1)/(L - 1)$ ; Corollary 4.2 shows the population-risk discrepancy between 1–1 and AR training is  $\Theta(L^T)$  for  $L > 1$ , mathematically explaining the catastrophic 1–1 failure in gas saturation.

**PINO stability (Section 6).** Theorem 6.5 shows PINO training with  $\lambda_R \geq \lambda_R^*$  reduces the operator spectral radius to  $\rho_{\mathcal{F}} + \mathcal{O}(\lambda_R^{-1/2}) < 1$ ; Theorem 6.6 shows physics residuals act as spectral Jacobian regularizers with error  $\mathcal{O}(\lambda_R^{-1/2})$ ; Theorem 6.7 gives uniform-in-time rollout error bounds  $\varepsilon/(1 - \rho)$  for PINO AR operators.

**TBPTT (Section 7).** Theorem 7.3 establishes geometric bias decay  $\mathcal{O}(\rho^K)$ ; Corollary 7.4 derives optimal window  $K^* = \mathcal{O}(\log T)$ ; Proposition 7.5 gives Adam convergence rate  $\mathcal{O}(1/\sqrt{t}) + \mathcal{O}(\rho^{K^*})$ .

**Empirical validation (Section 11).** Autoregressive PINO surrogates maintain  $R^2 > 0.99$  (oil),  $R^2 > 0.90$  (gas),  $R^2 \approx 0.80$  (pressure), and monotone improvement (water) across the full Norne 3298-day horizon; 1–1 models fail on gas and pressure. Ensemble inference runs in  $< 1$  minute on a single B200 GPU: a  $\sim 10^4 \times$  wall-clock speedup over the OPM finite-volume simulator.

Future work includes: (a) extending the Wasserstein covariate-shift bounds to non-Markovian (multi-step conditioning) operator inputs; (b) extending the PINO stability theorem to non-coercive residuals (e.g., hyperbolic-only without capillary regularization); (c) sharp Rademacher complexity bounds for FNO function classes via their spectral structure.

## Acknowledgments

This work was supported by NVIDIA Corporation. The authors also thanks **Harpreet Sethi** (NVIDIA Corporation) for his expert guidance and deep technical insights in reservoir simulation and physics-informed machine learning, which greatly benefited this work.

## References

- [1] Aziz, K., & Settari, A. (1979). *Petroleum Reservoir Simulation*. Applied Science Publishers.
- [2] Bartlett, P. L., & Mendelson, S. (2002). Rademacher and Gaussian complexities: Risk bounds and structural results. *Journal of Machine Learning Research*, 3, 463–482.
- [3] Bengio, Y., Simard, P., & Frasconi, P. (1994). Learning long-term dependencies with gradient descent is difficult. *IEEE Transactions on Neural Networks*, 5(2), 157–166.
- [4] Bengio, S., Vinyals, O., Jaitly, N., & Shazeer, N. (2015). Scheduled sampling for sequence prediction with recurrent neural networks. *Advances in Neural Information Processing Systems*, 28.
- [5] Bi, K., Xie, L., Zhang, H., Chen, X., Gu, X., & Tian, Q. (2023). Accurate medium-range global weather forecasting with 3D neural networks. *Nature*, 619, 533–538.
- [6] Chandra, A., Koch, M., Pawar, S., Panda, A., Azzizadenesheli, K., Snippe, J., et al. (2025). Accelerating porous media flow simulations with Fourier neural operators. *Advanced Theory and Simulations*, e00747.
- [7] Chen, T., & Chen, H. (1995). Universal approximation to nonlinear operators by neural networks. *IEEE Transactions on Neural Networks*, 6(4), 911–917.
- [8] Chen, Z., Huan, G., & Ma, Y. (2006). *Computational Methods for Multiphase Flows in Porous Media*. SIAM.
- [9] Equinor ASA. (2012). Norne Field Open Data Set. Open Porous Media Initiative. [https://opm-project.org/?page\\_id=559](https://opm-project.org/?page_id=559).

- [10] Etienam, C., Juntao, Y., Said, I., Ovcharenko, O., et al. (2024). A novel AI-enhanced reservoir characterization with a combined mixture of experts–NVIDIA Modulus based PINO forward model. *arXiv:2404.14447*.
- [11] Etienam, C., Juntao, Y., Ovcharenko, O., & Said, I. (2024). Reservoir history matching of the Norne field with generative exotic priors and a coupled MoE–PINO forward model. *arXiv:2406.00889*.
- [12] Etienam, C., Juntao, Y., Said, I., & Ovcharenko, O. (2024). A reservoir history matching approach using a coupled MoE-PINO forward model. *ECMOR 2024*, 1–35.
- [13] Herde, M., Raonic, B., Rohner, T., Käppeli, R., Mishra, S., de Bezenac, E., & Koumoutsakos, P. (2024). Poseidon: Efficient foundation models for PDEs. *arXiv:2405.19101*.
- [14] Karniadakis, G. E., Kevrekidis, I. G., Lu, L., Perdikaris, P., Wang, S., & Yang, L. (2021). Physics-informed machine learning. *Nature Reviews Physics*, 3, 422–440.
- [15] Kochkov, D., Smith, J. A., Alieva, A., Wang, Q., Brenner, M. P., & Hoyer, S. (2021). Machine learning–accelerated computational fluid dynamics. *Proceedings of the National Academy of Sciences*, 118(21).
- [16] Kovachki, N., Li, Z., Liu, B., Azizzadenesheli, K., Bhattacharya, K., Stuart, A., & Anandkumar, A. (2021). Neural operator: Learning maps between function spaces. *arXiv:2108.08481*.
- [17] Lam, R., Sanchez-Gonzalez, A., Willson, M., et al. (2023). Learning skillful medium-range global weather forecasting. *Science*, 382, 1416–1421.
- [18] Lamb, A. M., Goyal, A., Zhang, Y., Zhang, S., Courville, A. C., & Bengio, Y. (2016). Professor forcing: A new algorithm for training recurrent networks. *Advances in Neural Information Processing Systems*, 29.
- [19] Lanthaler, S., Mishra, S., & Karniadakis, G. E. (2022). Error estimates for DeepONets: A deep learning framework in infinite dimensions. *Transactions of Mathematics and Its Applications*, 6(1).
- [20] Li, Z., Kovachki, N., Azizzadenesheli, K., Liu, B., Bhattacharya, K., Stuart, A., & Anandkumar, A. (2020). Fourier neural operator for parametric partial differential equations. *arXiv:2010.08895*.
- [21] Li, Z., Zheng, H., Kovachki, N., Jin, D., Chen, H., Liu, B., Azizzadenesheli, K., & Anandkumar, A. (2021). Physics-informed neural operator for learning partial differential equations. *arXiv:2111.03794*.
- [22] Lu, L., Jin, P., Pang, G., Zhang, Z., & Karniadakis, G. E. (2021). Learning nonlinear operators via DeepONet. *Nature Machine Intelligence*, 3, 218–229.
- [23] Mikhaeil, J. M., Monfared, Z., & Durstewitz, D. (2022). On the difficulty of learning chaotic dynamics with RNNs. *Advances in Neural Information Processing Systems*, 35.
- [24] Mukundakrishnan, K., Wiegand, K., Natoli, V., Etienam, C., et al. (2024). Accelerating reservoir modeling workflows with neural operators and GPU-based simulations. *ADIPEC 2024*, D021S068R002.
- [25] Rasmussen, A. F., Sandve, T. H., Bao, K., et al. (2021). The Open Porous Media Flow reservoir simulator. *Computers & Mathematics with Applications*, 81, 159–185.
- [26] Pascanu, R., Mikolov, T., & Bengio, Y. (2013). On the difficulty of training recurrent neural networks. *ICML 2013*, 1310–1318.
- [27] Pathak, J., Subramanian, S., Harrington, P., et al. (2022). FourCastNet: A global data-driven high-resolution weather model. *arXiv:2202.11214*.
- [28] Peaceman, D. W. (1977). *Fundamentals of Numerical Reservoir Simulation*. Elsevier.
- [29] NVIDIA PhysicsNeMo. (2023). *GitHub*. <https://github.com/NVIDIA/physicsnemo>.
- [30] Raissi, M., Perdikaris, P., & Karniadakis, G. E. (2019). Physics-informed neural networks. *Journal of Computational Physics*, 378, 686–707.
- [31] Ranzato, M., Chopra, S., Auli, M., & Zaremba, W. (2016). Sequence level training with recurrent neural networks. *ICLR 2016*.
- [32] Rwechungura, R., Sjetne, O., & Lien, M. (2011). Application of advanced history matching techniques to the Norne field. *SPE Reservoir Simulation Symposium*.
- [33] Takamoto, M., Praditia, T., Leiteritz, R., et al. (2022). PDEBench: An extensive benchmark for scientific machine learning. *Advances in Neural Information Processing Systems*, 35.
- [34] Tallec, C., Ollivier, Y., & Chrisman, O. (2017). Unbiasing truncated backpropagation through time. *arXiv:1705.08209*.
- [35] Tang, M., Liu, Y., & Durlofsky, L. J. (2020). A deep-learning-based surrogate model for CO<sub>2</sub> storage. *International Journal of Greenhouse Gas Control*, 100, 103096.

- [36] Um, K., Brand, R., Fei, Y., Holl, P., & Thuerey, N. (2020). Solver-in-the-loop: Learning from differentiable physics. *Advances in Neural Information Processing Systems*, 33.
- [37] Venkatraman, A., Hebert, M., & Bagnell, J. A. (2015). Improving multi-step prediction of learned time series models. *AAAI 2015*.
- [38] Villani, C. (2009). *Optimal Transport: Old and New*. Springer.
- [39] Williams, R. J., & Zipser, D. (1989). A learning algorithm for continually running fully recurrent neural networks. *Neural Computation*, 1, 270–280.
- [40] Zygmund, A. (2002). *Trigonometric Series*, 3rd ed. Cambridge University Press.
- [41] Zhu, Y., & Zabaras, N. (2018). Bayesian deep convolutional encoder–decoder networks for surrogate modeling. *Journal of Computational Physics*, 366, 415–447.